









Review

A Review of the Phyllosilicates in Gale Crater as Detected by the CheMin Instrument on the Mars Science Laboratory, Curiosity Rover

Valerie M. Tu ^{1,*}, Elizabeth B. Rampe ², Thomas F. Bristow ³, Michael T. Thorpe ¹, Joanna V. Clark ⁴, Nicholas Castle ⁵, Abigail A. Fraeman ⁶ , Lauren A. Edgar ⁷ , Amy McAdam ⁸, Candice Bedford ⁹, Cherie N. Achilles ⁸, David Blake ³ , Steve J. Chipera ⁵, Patricia I. Craig ⁵ , David J. Des Marais ³, Gordon W. Downs ¹⁰, Robert T. Downs ¹⁰, Valerie Fox ¹¹, John P. Grotzinger ¹¹, Robert M. Hazen ¹² , Douglas W. Ming ², Richard V. Morris ², Shaunna M. Morrison ¹² , Betina Pavri ⁶, Jennifer Eigenbrode ⁸, Tanya S. Peretyazhko ¹, Philippe C. Sarrazin ¹³, Brad Sutter ¹, Allan H. Treiman ⁹, David T. Vaniman ⁵ , Ashwin R. Vasavada ⁶, Albert S. Yen ⁶ and John C. Bridges ¹⁴ 

- ¹ Jacobs Technology, NASA Johnson Space Center, Houston, TX 77058, USA; michael.t.thorpe@nasa.gov (M.T.T.); tanya.peretyazhko@nasa.gov (T.S.P.); brad.sutter-2@nasa.gov (B.S.)
 - ² NASA Johnson Space Center, Houston, TX 77058, USA; elizabeth.b.rampe@nasa.gov (E.B.R.); douglas.w.ming@nasa.gov (D.W.M.); richard.v.morris@nasa.gov (R.V.M.)
 - ³ NASA Ames Research Center, Moffett Field, CA 94035, USA; thomas.f.bristow@nasa.gov (T.F.B.); david.blake@nasa.gov (D.B.); david.j.desmarais@nasa.gov (D.J.D.M.)
 - ⁴ GeoControls Systems Inc—Jacobs JETS Contract at NASA Johnson Space Center, Houston, TX 77058, USA; joanna.v.clark@nasa.gov
 - ⁵ Planetary Science Institute, Tucson, AZ 85719, USA; nicholas.castle@gmail.com (N.C.); steve.chipera@gmail.com (S.J.C.); pcraig@psi.edu (P.I.C.); dvaniman@psi.edu (D.T.V.)
 - ⁶ Jet Propulsion Laboratory, California Institute of Technology, Pasadena, CA 91109, USA; abigail.a.fraeman@jpl.nasa.gov (A.A.F.); betina@jpl.nasa.gov (B.P.); ashwin.r.vasavada@jpl.nasa.gov (A.R.V.); albert.s.yen@jpl.nasa.gov (A.S.Y.)
 - ⁷ USGS Astrogeology Science Center, Flagstaff, AZ 86001, USA; ledgar@usgs.gov
 - ⁸ NASA Goddard Space Flight Center, Greenbelt, MD 20771, USA; amy.mcadam-1@nasa.gov (A.M.); cherie.n.achilles@nasa.gov (C.N.A.); jennifer.l.eigenbrode@nasa.gov (J.E.)
 - ⁹ The Lunar and Planetary Institute, Houston, TX 77058, USA; candice.c.bedford@nasa.gov (C.B.); treiman@lpi.usra.edu (A.H.T.)
 - ¹⁰ Department of Geosciences, University of Arizona, Tucson, AZ 85721, USA; gordie1997@gmail.com (G.W.D.); rdowns@arizona.edu (R.T.D.)
 - ¹¹ Division of Geology and Planetary Science, California Institute of Technology, Pasadena, CA 91125, USA; vfox@umn.edu (V.F.); grotz@gps.caltech.edu (J.P.G.)
 - ¹² Carnegie Institute for Science, Washington, DC 20015, USA; rhazen@carnegiescience.edu (R.M.H.); smorrison@carnegiescience.edu (S.M.M.)
 - ¹³ SETI Institute, Mountain View, CA 94043, USA; philippe.sarrazin@examintart.com
 - ¹⁴ University of Leicester, Leicester LE1 7RH, UK; jcb36@leicester.ac.uk
- * Correspondence: valerie.m.tu@nasa.gov; Tel.: +1-702-715-8632



Citation: Tu, V.M.; Rampe, E.B.; Bristow, T.F.; Thorpe, M.T.; Clark, J.V.; Castle, N.; Fraeman, A.A.; Edgar, L.A.; McAdam, A.; Bedford, C.; et al. A Review of the Phyllosilicates in Gale Crater as Detected by the CheMin Instrument on the Mars Science Laboratory, Curiosity Rover. *Minerals* **2021**, *11*, 847. <https://doi.org/10.3390/min11080847>

Academic Editor: Dominic Papineau

Received: 1 June 2021

Accepted: 24 July 2021

Published: 6 August 2021

Publisher's Note: MDPI stays neutral with regard to jurisdictional claims in published maps and institutional affiliations.



Copyright: © 2021 by the authors. Licensee MDPI, Basel, Switzerland. This article is an open access article distributed under the terms and conditions of the Creative Commons Attribution (CC BY) license (<https://creativecommons.org/licenses/by/4.0/>).

Abstract: *Curiosity*, the Mars Science Laboratory (MSL) rover, landed on Mars in August 2012 to investigate the ~3.5-billion-year-old (Ga) fluvio-lacustrine sedimentary deposits of Aeolis Mons (informally known as Mount Sharp) and the surrounding plains (Aeolis Palus) in Gale crater. After nearly nine years, *Curiosity* has traversed over 25 km, and the Chemistry and Mineralogy (CheMin) X-ray diffraction instrument on-board *Curiosity* has analyzed 30 drilled rock and three scooped soil samples to date. The principal strategic goal of the mission is to assess the habitability of Mars in its ancient past. Phyllosilicates are common in ancient Martian terrains dating to ~3.5–4 Ga and were detected from orbit in some of the lower strata of Mount Sharp. Phyllosilicates on Earth are important for harboring and preserving organics. On Mars, phyllosilicates are significant for exploration as they are hypothesized to be a marker for potential habitable environments. CheMin data demonstrate that ancient fluvio-lacustrine rocks in Gale crater contain up to ~35 wt. % phyllosilicates. Phyllosilicates are key indicators of past fluid–rock interactions, and variation in the structure and composition of phyllosilicates in Gale crater suggest changes in past aqueous environments that may have been habitable to microbial life with a variety of possible energy sources.

Keywords: clay minerals; phyllosilicates; organic preservation; Mars; gale crater; X-ray diffraction; Mars Science Laboratory; CheMin

1. Introduction

The Mars Science Laboratory (MSL) *Curiosity* rover landed on Mars in August 2012 in Gale crater (Figure 1), an impact basin ~155 km in diameter that formed ~3.8 Ga before present during the late Noachian epoch [1]. The rover was sent to investigate a 5-km high mound of layered sedimentary rock, located in the center of Gale crater, Aeolis Mons (informally known as Mount Sharp), and to determine the potential for habitable environments in the past and present day [2]. Based on orbital visible/shortwave infrared (VSWIR) reflectance spectroscopy, some of the layers on the lower slopes of Mount Sharp show variations in mineralogy thought to record environmental changes over time [3]. Orbital defined mineralogical units have been identified using VSWIR and include the deep spectral absorptions for a phyllosilicate-bearing unit, hematite ridge, (i.e., Vera Rubin Ridge (VRR)) and sulfate-bearing unit. After landing on the plains (Aeolis Palus) of Gale crater at Bradbury Landing, *Curiosity* drove ~500 m east to an embayment on the floor of Gale crater to explore the fluvio-lacustrine strata at Yellowknife Bay (YKB), which lie at the lowest elevation point and represent the oldest rocks that *Curiosity* has studied (Figure 2) [4]. The rover then headed southwest across the plains around an active aeolian dune field and turned to the south to begin its investigation of the lower layers of Mount Sharp, starting in September 2014. During its extensive journey, *Curiosity* discovered evidence for a lake or series of lakes that once filled Gale crater that likely persisted for millions of years [5–9].



Figure 1. Gale crater is 155-km in diameter and contains a 5-km high mound of stratified rock. Strata in the lower section of the mound vary in mineralogy and texture, suggesting that they may have recorded environmental changes over time. The yellow oval denotes the MSL landing ellipse and the star denotes the landing site. Image credit: NASA/JPL-Caltech/ESA/DLR/FU Berlin/MSSS. (accessed on 23 July 2021).

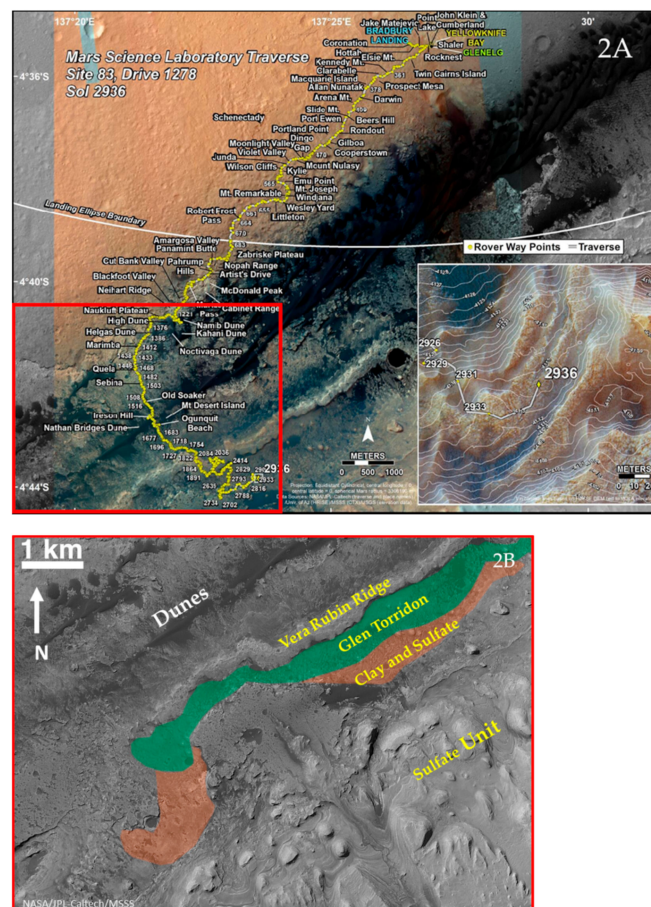


Figure 2. (A) Mars Science Laboratory (MSL) traverse (yellow line) through strata heading southwest across the Gale crater plains towards the base of Mount Sharp, then heading south/southeast up the lower slopes of Mount Sharp. The inset shows a close-up of *Curiosity* location at the time of writing, overlain with elevation. (B) High Resolution Imaging Science Experiment (HiRISE) mosaic showing the major units of Gale crater as identified and mapped through orbital mineralogy observation, including the hematite-bearing Vera Rubin ridge (VRR), the Clay unit (Glen Torridon), Clay and Sulfate unit, and the Sulfate unit (all image credits: NASA/JPL-Caltech/MSSS/JHUAPL/Brown University).

Lower Mount Sharp comprises sedimentary rocks that are ~3.5 billion years (Ga) old and contain fluvio-lacustrine mudstones with up to ~35 weight % phyllosilicates in the bulk rock [10–12]. To date, *Curiosity* has investigated ~400 m of vertical stratigraphy from Yellowknife Bay through Glen Torridon (GT). As of March 2021, the rover is investigating a transition between GT and the stratigraphically higher sulfate-bearing unit (Figure 2) to complete one of its longstanding scientific objectives, to assess the “habitability” of Mars [2] with a key region of interest being the layered phyllosilicate-bearing deposits that outcrop in the lower NW slopes of Mount Sharp.

Phyllosilicate-bearing layers are desirable targets for investigation on Mars given their potential to enhance the preservation of organics [13–18] and serve as indicators of wetter surficial conditions in the past [2,4,10,13,19–25]. To investigate the phyllosilicates in Gale crater, drilled rock powders and scooped samples of loose sediment are measured by the Chemistry and Mineralogy (CheMin) X-ray diffractometer. Results from the CheMin instrument provide definitive mineralogy and abundances of phases from martian surface materials [26], which include a variety of phyllosilicates in almost all drilled rock samples to date. The identity of these phyllosilicates helps reveal the history of liquid water in Gale crater.

Water is incorporated into sediments, soils, and rocks through adsorption, physically trapping water in confined pore spaces or at grain boundaries, via solvation, as part of the structural make-up of minerals (“hydrous minerals”) (e.g., [27]). Phyllosilicates (frequently referred to as clays or clay minerals) are hydrous minerals that commonly form as a result of water-rock interactions and contain H₂O and/or OH as part of their structure. The term ‘clay’ is often used interchangeably to describe a grain size fraction and as a mineralogical group (i.e., phyllosilicates), making it challenging to distinguish in literature. Phyllosilicates inherently have a small grain size and are naturally occurring materials, including soil, sediment, or rock. Whereas clay may contain phyllosilicates, it may also contain other materials that impart plasticity and harden when dried or fired [28]. Hydroxyl groups are bound within octahedral sheets in the phyllosilicate structure, and water molecules solvate cations, such as Na⁺, K⁺, and Ca²⁺, in the interlayers of swelling clay minerals (i.e., smectite and vermiculite) (Figure 3).

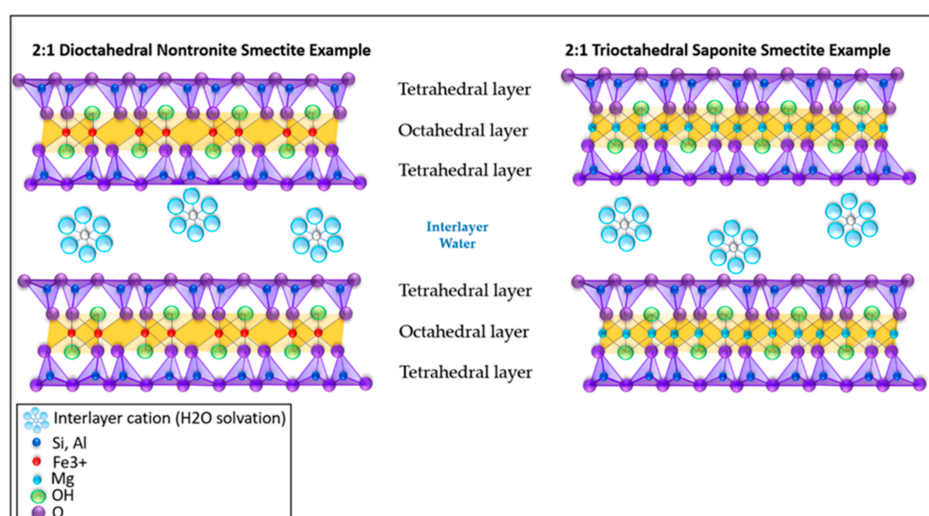


Figure 3. An example of the structure of dioctahedral nontronite and trioctahedral saponite demonstrating tetrahedral and octahedral layers (2:1), connected by hydroxyl groups and apical oxygens. In between the tetrahedral-octahedral-tetrahedral (TOT) sheets, in the interlayer site, cations are exchanged and H₂O is adsorbed. Both of these phyllosilicates have been observed at Gale crater.

The phyllosilicate mineral group is structurally and compositionally diverse, and their structures are sensitive to changes in environmental conditions. On Earth, a wide variety of phyllosilicates are observed, including smectite, kaolinite, chlorite, and illite, where the phyllosilicate structure and composition depend on the aqueous conditions at the time of formation (e.g., pH, temperature, salinity) and the parent material, in addition to potential subsequent diagenetic conditions and processes. Smectites are common in a variety of environments and typically form at relatively low temperatures in poorly drained soils [29,30], in alkaline or saline lakes [31], and from deuteric alteration of basalts, and by the alteration of volcanic ash deposits [32]. The type of smectite (e.g., saponite, montmorillonite, nontronite) is controlled by the parent material, degree of alteration, and the salinity and pH of the fluids (e.g., [29,30,33]). Kaolinite is common in well-drained soils that experience enhanced leaching. Illite and chlorite often form at mildly elevated temperatures during burial diagenesis or contact metamorphism, or at surface temperatures in saline and alkaline lakes [29,31,33].

Smectites are the main type of phyllosilicate observed on Mars from orbit [34,35]. Trioctahedral ferric saponite has also been observed in olivine fractures of the nakhlite martian meteorite, Lafayette [36]. The smectite structure includes two Si,Al-O tetrahedral sheets sandwiching a M^{2+,3+}-O,OH octahedral sheet, with Al³⁺, Mg²⁺, Fe³⁺, and Fe²⁺, typically serving as the octahedral cation (Figure 3). They are characterized by their ability

to adsorb H₂O in their interlayer sites and expand and collapse depending on the relative humidity, layer charge, and cations present in their interlayers (e.g., Na, Ca, Mg, Fe) [37].

Phyllosilicates are ideal targets for investigations of organics on Mars, as they have a negative electrostatic layer charge and high surface area that attracts and helps preserve organic compounds in the rock record [38–40]. Clay-rich, fine-grained lacustrine deposits are considered prime targets for the investigation of organics on Mars [13,14]. Here, we review the phyllosilicates that have been detected in Gale crater by the CheMin instrument with constraints provided by the SAM, APXS and ChemCam instruments on-board *Curiosity* through ~sol 3000 (i.e., 3000 martian days). We describe the implication these phyllosilicate detections have on past aqueous environments, alteration and diagenesis, and the preservation of organics.

2. Background

2.1. Orbital Phyllosilicate Detections on Mars

Phyllosilicates have been detected from orbit across much of Mars using (VSWIR) imaging spectrometers and are associated with Mars's oldest terrain (~4 Gyr., Noachian-aged) (e.g., [19–21,24,41]) (Figure 4). These minerals are identified by overtones and combinations of fundamental vibrational absorption features between 1 and 2.6 μm . Interlayer H₂O is associated with a 1.9 μm absorption caused by a combination band of the fundamental bending and stretching vibrations of water. An overtone absorption is resonant with the fundamental absorption. Overtones are generally associated with shallower absorptions than fundamental absorptions. Combination bands of H₂O molecules and overtones of OH also cause absorptions at 1.4 μm [42]. Metal-OH combination stretching plus bending vibrations occur from 2.2 to 2.4 μm , and the position of the absorption center depends on the octahedral cations (Fe^{2+,3+}, Mg²⁺, Al³⁺) that are present, as well as the mineral structure. Fe³⁺-OH absorptions in smectite are found near 2.28 μm , and Mg-OH absorptions shift to 2.31 μm . Most Fe/Mg phyllosilicates on Mars are characterized by an absorption 2.30 μm that is generally interpreted to represent a mix of ferric and magnesian phyllosilicate species [22]. Although less commonly observed on Mars, aluminous smectites are characterized by Al-OH absorptions found near 2.20 μm [43].

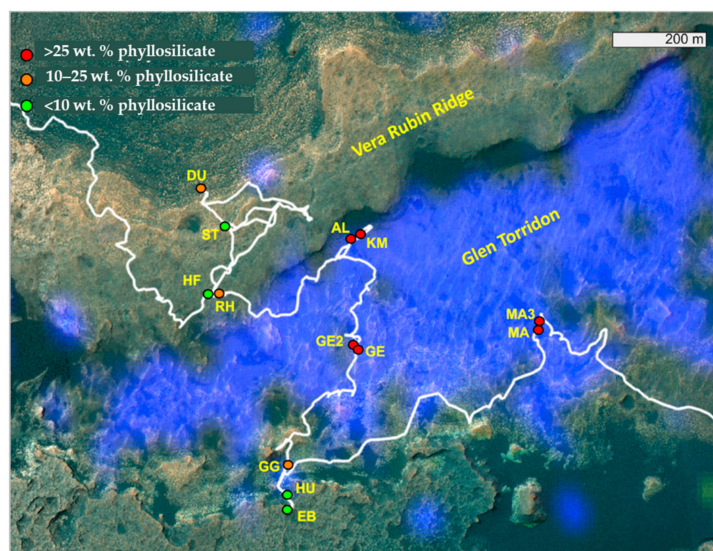


Figure 4. Compact Reconnaissance Imaging Spectrometer for Mars (CRISM) map of Fe/Mg-smectite spectral absorptions detections from orbit in the Glen Torridon region of Gale crater with the darkest blue representing the deepest spectral absorptions attributed to phyllosilicate (map courtesy Valerie Fox), and with drill holes reflecting CheMin phyllosilicate abundances. Red circles, phyllosilicate abundances greater than 25 wt. %. Orange circles, phyllosilicate abundances 10–25 wt. %. Green circles, represent phyllosilicate abundances <10 wt. %.

From orbit, phyllosilicates are found in a variety of geologic settings that can be loosely categorized into three broad classes: (1) associated with the central peaks, walls, and ejecta of impact craters; (2) in-place in stratigraphies that suggest formation in situ; and (3) sedimentary basins [21,34,35].

Orbital observations are essential for determining the mineralogy of the large-scale surface of Mars, but mineral detections are impacted by dust coverage and the spatial resolution of orbital imaging spectrometers, which at best are 10s of meters per pixel. The presence of outcrops with orbital absorptions attributed to phyllosilicates has motivated the selection of five landing sites that have or will be explored by rovers. Weak absorptions attributed to both Fe/Mg and Al smectites are present in the Columbia Hills at Spirit's landing site in Gusev Crater [44]. Absorptions attributed to Fe/Mg smectites are also present at Opportunity's exploration sites at the Cape York and Marathon Valley segments along the rim of Endeavour crater [22,45]. Fe/Mg smectites with Al-substitution are also mapped in the lowermost strata of Mount Sharp in *Curiosity's* exploration site at Gale crater, and the densest and deepest spectral absorptions are seen in Glen Torridon (Figure 4) [3]. Fe/Mg smectites are also seen associated with delta deposits at Jezero crater, the landing site of the Perseverance rover [13]. Finally, phyllosilicate signatures are present at Oxia Planum, the proposed future landing site of the European Space Agency's (ESA) ExoMars rover "Rosalind Franklin," and they are hypothesized to have formed in one of two distinct aqueous environments during the Noachian [46].

2.2. Stratigraphy from *Curiosity's* Traverse

Since landing in August 2012, *Curiosity* has gained more than 400 m of elevation, and has documented stratigraphy along its traverse. In order to track the sedimentary facies and changing depositional environments as *Curiosity* ascends Mount Sharp, the team developed a working stratigraphic column (Figures 5 and A1). This column represents a log of the lithologies and relationships between stratigraphic units along the traverse path, and therefore accounts for considerable lateral distance and should not be interpreted as a true vertical succession at any one location. However, this column is useful for tracking changes in deposition and chemostratigraphic/mineralogic trends.

Over the ~9 years since landing, *Curiosity* has investigated a variety of siliciclastic sedimentary rocks in Gale crater. *Curiosity* identified a conglomerate with well-rounded pebbles near the landing site, consistent with fluvial deposition [47]. The YKB formation 500 m east of the landing site includes a meter scale outcrop of phyllosilicate-bearing mudstones, interpreted to record an ancient habitable, lacustrine environment [4]. As *Curiosity* drove southward and gained elevation, the rover encountered fluvial and deltaic facies [5,47,48] before reaching a thick succession of dominantly fine-grained, well-laminated rocks, known as the Murray formation, at the base of Mount Sharp. The Murray formation accounts for more than 370 m of vertical section investigated by *Curiosity* and consists mainly of mudstones that were deposited in lake and lake margin settings (e.g., [5,6,8,9,49,50]). The Murray formation is divided into nine stratigraphic members based on facies variations, which help to track the evolution of the conditions and depositional environments of the lake basin preserved in the rock record. While much of the Murray formation represents a lacustrine environment (suitable for the formation of phyllosilicates), this record of low-energy deposition was occasionally interrupted by plunging river plumes [6], desiccation [51], and aeolian or fluvial deposition around the lake margin [7,52]. The Murray formation is unconformably overlain by ancient aeolian sandstones known as the Stimson formation [53] (Figures 5 and A1). *Curiosity* studied the Stimson formation at locations known as the Naukluft and Emerson plateaus, Murray buttes, and the Greenheugh pediment capping unit.

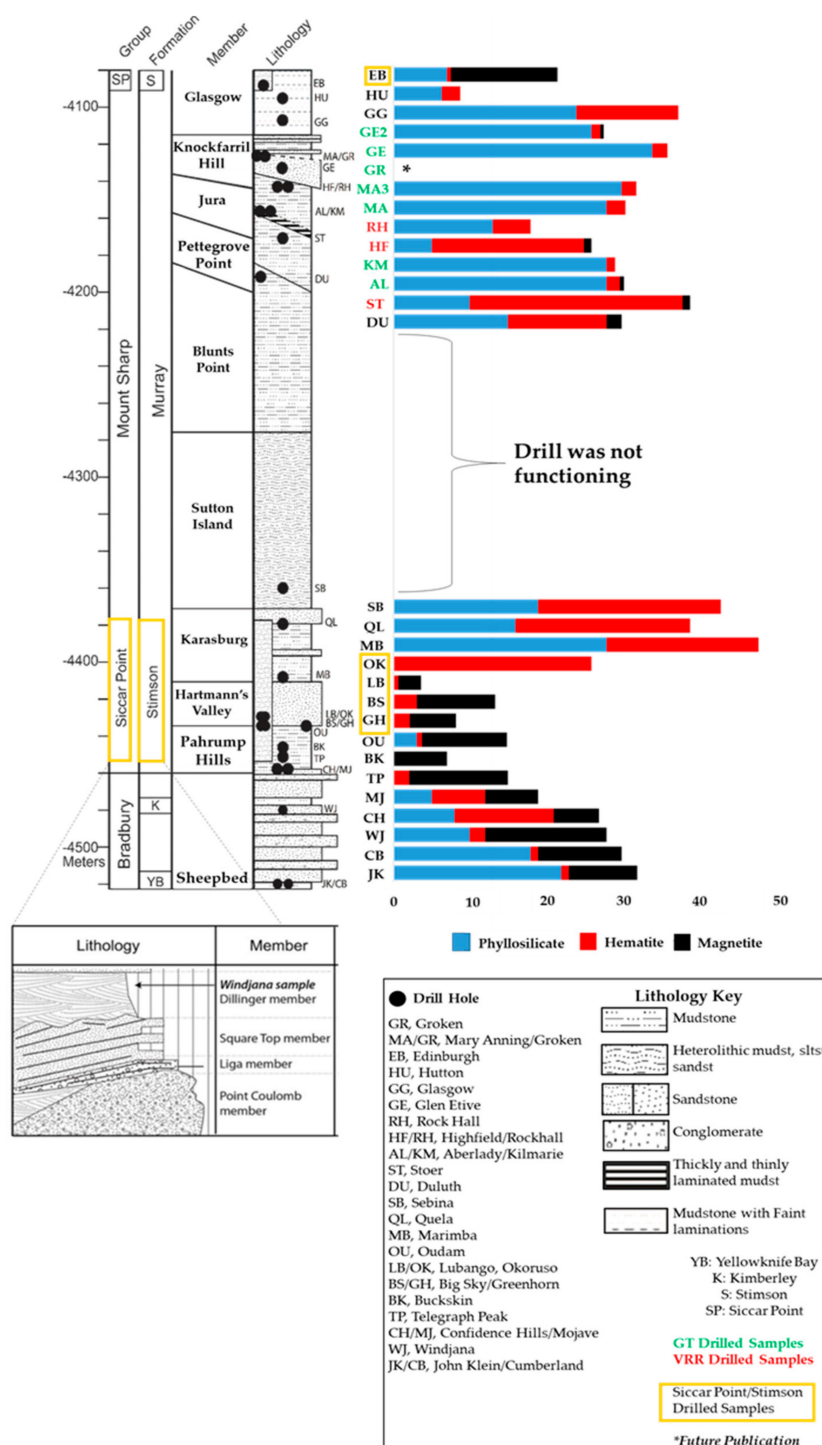


Figure 5. Stratigraphic column of the sedimentary rocks at Gale crater from the MSL sedimentary and stratigraphy working group. The stratigraphic column reflects the units and formations investigated by *Curiosity* from the landing site near Yellowknife Bay through the Murray formation, Glasgow member. Modified enlarged inset of the Kimberley formation, showing the location of the WJ sample drilled in the Dillinger member [54]. Next to the column are phyllosilicate abundances of each of the drilled samples (blue bars), hematite (red bars), and magnetite (black bars) and Glen Torridon, Vera Rubin Ridge, and Siccar Point group samples are denoted, in addition to the drilling hiatus. * Sample GR mineral abundances are currently being assessed by the CheMin team and will be released in an upcoming publication.

2.3. Habitability and Microbial Organisms

Phyllosilicates play an important role in preserving organic matter in rocks on Earth and are important indicators of ancient habitability on Mars [4,10,23]. Grotzinger [4] established the habitability of ancient lakes in Gale based around criteria and observations demonstrating clement aqueous conditions (moderate pH, T, salinity etc.), accessibility to biogenic elements (P, S, C, H, N), and potential metabolic energy sources (e.g., Fe oxidation). Bristow et al. [23] considered the importance of longevity of such clement conditions as an aspect of habitability more explicitly. Several microbial metabolic pathways have been hypothesized to have occurred in Mars' history [55–59], and here we briefly discuss some of those suggested to be relevant and important to potential microbial habitability at Gale crater, based primarily on mineral indicators of geochemical conditions.

On Earth, chemolithotropic microaerophiles utilize soluble Fe^{2+} as an energy source [60,61]. Bristow et al. [23] suggest that Fe-oxidizing microbes, such as *Pseudomonas* sp. HerB, identified from a lava-tube cave in Oregon, which use olivine derived Fe^{2+} as an energy source under low oxygen conditions [62], provide an example of organism that could have inhabited the lake environments of the type recorded by rocks exposed at YKB. Tosca et al. [63] suggest H_2 produced by aqueous alteration of olivine under anaerobic conditions on early Mars could have been utilized as a potential fuel for autotrophic metabolisms [64], such as acetyl coenzyme A, which is considered one of the earliest bioenergetics metabolisms on Earth [65,66].

Ancient Martian fluid-mixing zones, are another potential energy source for microbial life that may be relevant to Gale [55]. Kikuchi and Shibuya [55] hypothesize that energetically habitable environments could be present in areas where reduced ground water mix with oxidized surface water, creating redox gradients that could be mediated by microbes to obtain energy. Similar to other models, it is proposed that energy in these mixing zones could have been derived by biologically mediated oxidation of Fe^{2+} .

3. Materials and Methods

Phyllosilicate Detection Payload Instruments

CheMin Instrument: The CheMin X-ray diffractometer (Figure 6) is essential for identifying and quantifying the in-situ surface mineralogy of Gale crater, and here we provide a description of the CheMin instrument configuration, and the methodology for quantifying crystalline, amorphous, and phyllosilicate constituents in Martian rocks and sediments. CheMin is an X-ray diffractometer and X-ray fluorescence spectrometer that generates 2D XRD patterns of scooped sediment or rock powder drilled from between 2 and 6.5 cm depth. Up to sol 1536 (November 2016), samples were ingested to the Collection and Handling for In-Situ Martian Rock Analysis (CHIMRA) and sieved to a $<150 \mu\text{m}$ grain size. A $\sim 50 \text{ mg}$ portion of the sieved material was then dropped into CheMin's inlet funnel on the rover deck to deliver sample to a predetermined CheMin sample cell (out of 27 reusable cells). CheMin is configured in transmission geometry. Sediment or rock powder within a Mylar or Kapton cell is vibrated during analysis via piezo electric actuators to convectively move the sample as an X-ray beam generated from a cobalt source ($\lambda = 1.79027 \text{ \AA}$, averaged $k\alpha_1$ & $k\alpha_2$) penetrates the sample material. Diffracted X-ray photons are collected on a charge-coupled device (CCD) (Figure 6) [26]. CheMin has a collimated beam of $70 \mu\text{m}$ in diameter and an angular resolution of $\sim 0.25^\circ 2\theta$ and an angular range of $\sim 4\text{--}52^\circ 2\theta$ with data collected over 3–38 h [26,67]. *Curiosity* lost the use of its drill feed motor on sol 1536 and since then has used a method called “feed-extended drilling” or “feed-extended sample transfer”, which leaves the drill bit in a fully extended state [68]. In this configuration, delivery through CHIMRA is no longer possible and the sample is fed directly into the CheMin inlet by hovering the drill bit over the inlet using small amounts of reverse drill bit rotation and percussion to deliver the sample.

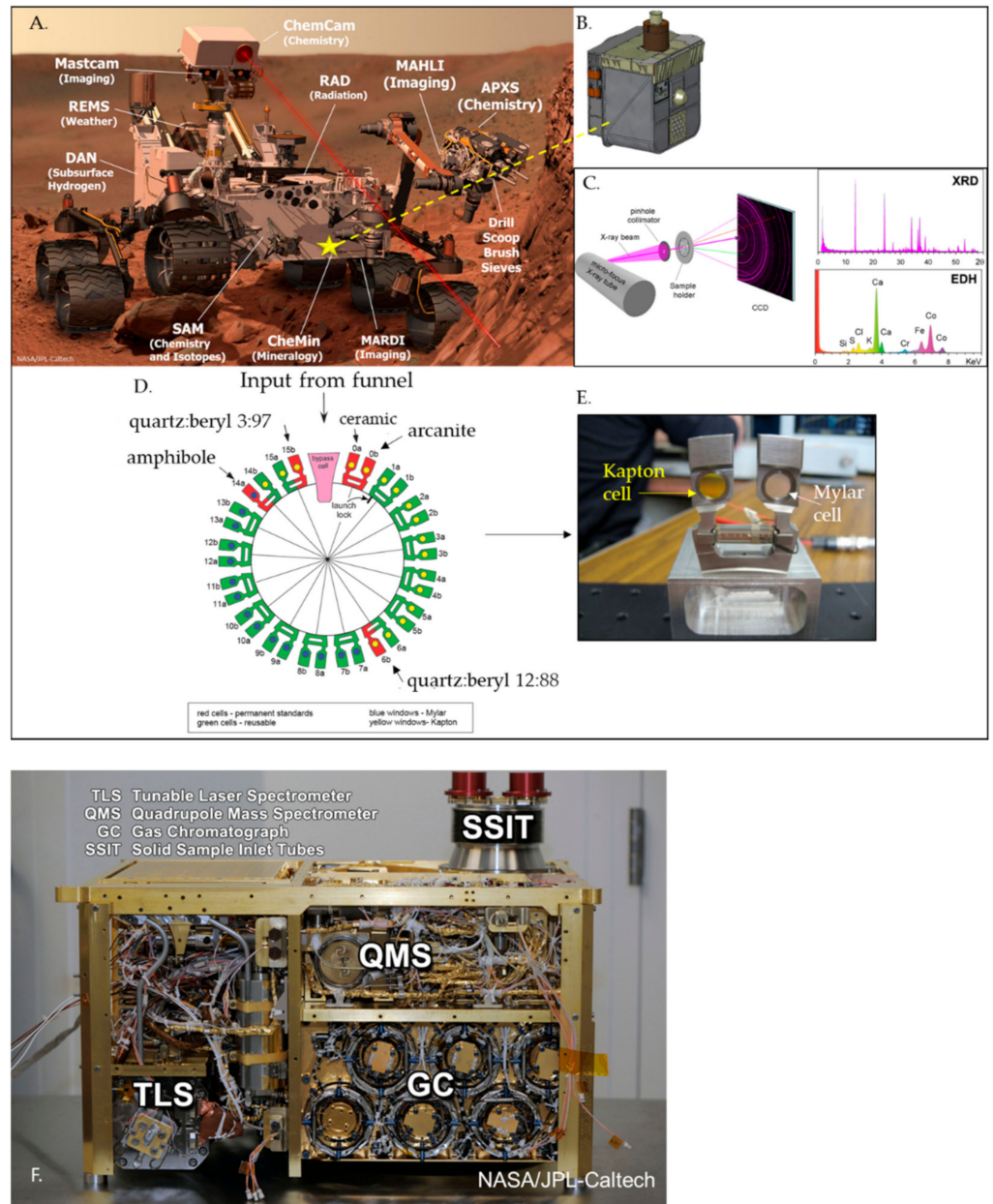


Figure 6. (A) *Curiosity* rover science payload with the CheMin instrument identified with a yellow star. CheMin and SAM instruments reside in the interior of *Curiosity* and have sample inlets that protrude through the top deck. Image credit: NASA/JPL-Caltech. (B) A schematic of the CheMin instrument (about the size of a laptop inside a carrying case). (C) A schematic demonstrating the basic components of CheMin which includes sample within a holder in transmission geometry with a cobalt X-ray source penetrating the sample. Diffracted X-rays are collected on a CCD, and the resulting 2D patterns are converted into a 1D pattern. (D) CheMin sample cell wheel that contains 27 reusable sample cells (green) and 5 standards (red). Of the reusable cells, 14 are Mylar (blue circles) and 13 are Kapton (yellow circles). (E) CheMin laboratory analog cells with Kapton (yellow) and Mylar cells (colorless) (B–E) [26]. (F) SAM Instrument suite that is about the size of a microwave oven, and the 3 instruments visible include: The tunable laser spectrometer (TLS) (lower left), quadrupole mass spectrometer (QMS) (upper right, and gas chromatograph (GC) (lower right). The solid sample inlet tubes (SSIT) is visible at the top right and is used for delivery by the robotic arm to deliver samples. Image credit: NASA/JPL-Caltech, accessed on 23 July 2021.

Martian mineral phase identification and the determination of abundances are a function of a robust process of data conversion and data analysis performed by numerous CheMin team members. The CheMin instrument generates 2D XRD patterns of samples and these patterns are converted into 1D patterns using a modified version of GSE_ADA software v1.09 [69], modified by P. Dera (University of Hawai'i). The resulting 1D patterns allow CheMin team members to perform phase identification and Rietveld refinements to determine mineral abundances and unit-cell parameters of major crystalline phases. Rietveld refinement is a technique used to model peak positions and intensities [70–72] by modifying the unit-cell parameters, peak widths, and scaling factors from crystallographic information files (CIFs) or crystalline phases. For crystalline phases the detection limit of CheMin is ~1 wt. %. Team members who refine the XRD diffraction patterns of Mars samples, referred to as 'fitters', determine non-phylosilicate (e.g., mafic minerals, feldspar, oxides, sulfates) and phyllosilicate phases present and model an amorphous hump, using the Materials Data Inc (MDI) software suite, Jade™ v9. Offsets are applied to 1D diffraction patterns to account for small differences in sample-to-detector distances that arise when using different sample cells by –25 to –113 μm relative to an ideal sample cell-to-CCD distance of 18.5302 μm [67]. The sample-to-detector difference causes shifts in the 2θ peak position of the XRD patterns which is corrected with an internal calibration method based on the refined cell parameters of plagioclase feldspar [73]. Morrison et al. [73] described equations capturing the relationships between unit-cell parameters and crystal chemistry for major mineral phases such as feldspar, pyroxene, and olivine allowing constraints to be placed on the chemistry of these minerals in Martian samples. Non-phylosilicate crystalline phase determination is typically easier than the determination of specific species of phyllosilicates because there is often a greater degree of freedom of substitutions that can take place in phyllosilicates, causing subtle changes in structure, and thus the XRD pattern. Moreover, some phyllosilicates can be poorly crystalline such that their XRD peaks are broad and asymmetrical. The identification of phyllosilicates in CheMin XRD patterns requires a more thorough assessment and comparison to XRD patterns of Mars-analog phyllosilicates collected or synthesized on Earth and measured in a CheMin-like instrument and is necessary because on Mars we cannot concentrate phyllosilicates through size fractionation nor perform routine chemical treatments to identify clay minerals in labs on Earth such as those by [74].

Phyllosilicate abundances are determined by the CheMin team using measured standard XRD patterns of terrestrial phyllosilicate samples that have been desiccated, purged in dry nitrogen gas and analyzed on a laboratory CheMin analog instrument to compare to the flown CheMin instrument results (e.g., [75]). On Mars, smectite basal spacings are expected to collapse under the low relative humidity conditions inside the CheMin instrument, making it difficult to distinguish illite from collapsed smectite. X-ray amorphous, poorly crystalline, and para-crystalline material abundances are determined using a modified version of the full pattern fitting program, FULLPAT, which contains a library of Mars relevant poorly crystalline materials (e.g., ferrihydrite, allophane, etc.) [76,77]. This program uses a least-squares minimization to fit the measured CheMin patterns using patterns of individual minerals, X-ray amorphous materials, and phyllosilicates [76,77]. Phyllosilicates are identified in CheMin XRD 1D patterns using their characteristic peaks (e.g., $d(001)$, $d(021)$). The $d(021)$ phyllosilicate peak is specifically sensitive to cation occupancy sites within the octahedral sheets of phyllosilicates (Figure 7) [11,33,74]. Although the CheMin instrument is the primary mineralogy instrument on-board *Curiosity*, collaboration with other MSL instruments such as the Sample Analysis at Mars (SAM), Chemistry and Camera (ChemCam), and Alpha-Particle X-ray Spectrometer (APXS) (Figure 6) aid in the interpretation of the type and presence of phyllosilicates through the use of chemical data, such as bulk K^+ to try and distinguish illite from collapsed smectite.

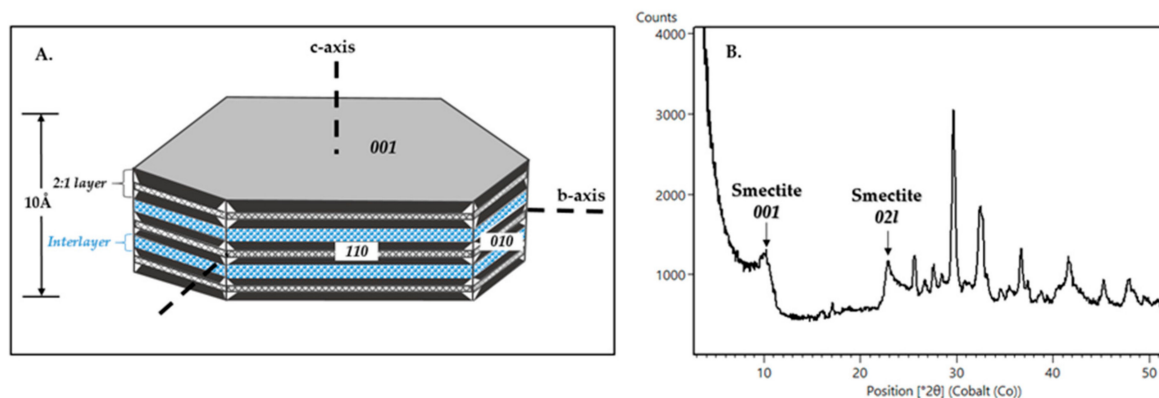


Figure 7. (A) Smectite structure demonstrating the c-axis and b-axis of a collapsed smectite structure with $d(001)$ at 10\AA . (B) CheMin XRD pattern from drilled martian sample “Glen Etive” (GE) from the Knockfarril Hill member of the Murray formation showing the $d(001)$ and $d(021)$ peaks.

SAM Instrument Suite: The SAM instrument (Figure 6) analyzes the chemical and isotopic chemical composition of the atmosphere and volatile-bearing phases in scooped or drilled surface materials. A key objective is to identify organics present in Gale sediments. Before the drill feed anomaly, CHIMRA delivered scooped or drilled samples to quartz or metal cups inside SAM’s Sample Manipulation System (SMS). With feed-extended drilling, the sample is delivered to SAM in a similar manner as to CheMin, where the drill bit is placed above the inlet and the rotation is reversed so that some material drops from the drill bit into the instrument. The cups are then transferred into one of SAM’s ovens, where they are heated from 35 to $\sim 870\text{ }^{\circ}\text{C}$ at a rate of $35\text{ }^{\circ}\text{C}/\text{min}$ [78–80]. The carrier gas is used to send evolved gases to a quadrupole mass spectrometer (QMS). After delivery to the QMS, evolved gases can then be sent to gas chromatograph (GC) columns or to the tunable laser spectrometer (TLS). Volatile-bearing phases, such as phyllosilicates, thermally decompose and evolve gases like H_2O . The types of evolved gases and the decomposition temperature can aid in phase identification. Like the CheMin team, the SAM team utilizes a laboratory analog instrument to take measurements of known mineral and phyllosilicate phases, for direct comparison to the flown SAM instrument for specific phyllosilicate identification.

The identity and temperature of evolved gases during SAM evolved gas analysis (EGA) can support CheMin mineral detection and inform the presence of trace volatile-bearing phases or phases difficult to characterize with X-ray diffraction, such as phyllosilicates and X-ray amorphous materials. Phyllosilicate octahedral layer properties (e.g., octahedral cations and position of octahedral vacancies) influence their temperatures of dehydroxylation and coincident H_2O evolution during heating. Generally, the dehydroxylation of trioctahedral phases occurs at higher temperatures than dioctahedral phases [81]. Peaks in SAM H_2O EGA data at temperatures greater than $\sim 400\text{ }^{\circ}\text{C}$ can provide constraints on the likely identity of phyllosilicates in a sample based on comparisons to the results of SAM-like laboratory EGA of relevant analog phyllosilicates.

In case CheMin detects a significant amount of phyllosilicates in a sample such that the phyllosilicate $d(021)$ peak can be readily observed/ modeled to infer possible phyllosilicate identity, peaks in SAM H_2O EGA data from the sample can help to confirm or potentially further constrain the phyllosilicate present. In the event that CheMin detects phyllosilicates but it is not possible, or is difficult, to observe the $d(021)$ peak, $>400\text{ }^{\circ}\text{C}$ H_2O evolutions in SAM EGA data can be a primary source of information on the possible identity of the phyllosilicate in the context of other data from the sample and sampling area (e.g., APXS bulk chemistry of the sample powder). In case CheMin does not detect evidence of phyllosilicates, H_2O peaks in SAM EGA at temperatures above $\sim 400\text{ }^{\circ}\text{C}$ can be used to infer the possible presence of phyllosilicates in a sample at abundances below CheMin detection limits, as long as consideration is given for other potential hydrous phases in the sample (e.g., jarosite).

ChemCam Instrument Suite: The ChemCam instrument suite includes the first Laser-Induced Breakdown Spectrometer (LIBS) on a planetary mission. It is coupled with a high-resolution remote microscope imager (RMI) to provide detailed context imaging before and after target analysis (Figure 6) [82,83]. A series of 14 mJ laser pulses is directed at a target between 2.2–7.0 m from the rover mast to create a weakly ionized plasma on the incident sample [82,83]. The strength and wavelength of the atomic emission spectrum of the plasma is then analyzed by three spectrometers in the ultra-violet (240–42 nm), visible violet (382–469 nm), and visible/near infrared (474–906 nm) spectral ranges [83]. The LIBS technique acquires major, minor, and some trace and halogen compositions at the submillimeter-scale (0.3–0.6 mm) of a geological target [82–85]. Geological targets are analyzed by a linear or grid raster pattern of observation points whereby each observation point consists of 30–50 spectral analyses. The repeated firing of the laser at an observation point on the target removes dust in the first five laser pulses with further pulses providing a sample depth profile [83]. RMI images are acquired before and after LIBS analyses to provide high-resolution context imaging at an optical resolution of ~40–50 μ rad [82,86]. Due to the rapid remote-sensing capabilities of the ChemCam instrument, >800,000 LIBS spectra have been acquired for thousands of targets along the *Curiosity* rover's traverse to date. This contrasts with the 30 drilled and three scooped samples analyzed by the CheMin instrument through sol 3064. As such, several studies have employed ChemCam LIBS elemental data alongside the mineralogical data provided by CheMin to trace phyllosilicate content and estimate the level of chemical weathering in the sedimentary rocks of Gale crater (e.g., [87–95]).

APXS Instrument: The APXS instrument on-board *Curiosity* (Figure 6) is an in-situ method of determining chemical composition of rocks and soils with X-ray fluorescence and particle-induced X-ray emission spectroscopy at the Martian surface [96,97]. Elemental abundances measured on rocks and drill powder samples can help CheMin constrain the composition of the X-ray amorphous component through mass balance calculations [98]. APXS uses a radioactive ^{244}Cm source to irradiate rocks or soil with high-energy alpha particles and X-rays, which produces X-ray emissions and X-ray fluorescence that are recorded with an energy-sensitive detector, and to detect all elements heavier than fluorine [96].

Similar to ChemCam, APXS does not detect phyllosilicates. Instead, APXS uses elemental abundances to inform the mineralogy of drilled samples, and chemical trends are assessed to interpret environmental changes and diagenetic fluid events. APXS is used in conjunction with CheMin to determine if a specific species of phyllosilicate is present, in particular to distinguish if illite versus smectite is present. Illite is a non-expanding, 2:1, K-rich phyllosilicate, and APXS potassium abundances are used to determine if illite is potentially present [11].

4. Limitations on Phyllosilicate Detection

Despite being equipped with the most sophisticated mineralogical instruments to fly to another planet, there are limitations in our ability to identify and quantify minerals. Here we review some of the known instrument limitations on analyzing and identifying phyllosilicates on Mars.

Miniaturizing an X-ray diffractometer for space flight results in a loss of angular range and resolution compared to laboratory instruments. CheMin measures an angular range of $5\text{--}52^\circ 2\theta$, unlike high-resolution laboratory instruments that typically measure from $2\text{--}100^\circ 2\theta$, and therefore does not include the (06l) diffraction peak, important for distinguishing a trioctahedral phyllosilicate at $\sim 1.54\text{--}1.52 \text{ \AA}$, ($\sim 71^\circ 2\theta \text{ Co K}\alpha$) from a dioctahedral phyllosilicate at $\sim 1.52\text{--}1.50 \text{ \AA}$ ($\sim 73^\circ 2\theta \text{ Co K}\alpha$) [10,74] (Figure 3). The d(02l) peak position at $\sim 22.5\text{--}23.1^\circ 2\theta \text{ Co K}\alpha$ can be used to distinguish dioctahedral and trioctahedral structures and derive the 'b' unit cell parameter (Figures 3 and 7). However, this diffraction peak is asymmetrical and is often overlapped by diffraction peaks from other mineral phases such as augite [10]. The angular resolution is $\sim 0.25^\circ 2\theta \text{ Co K}\alpha$, significantly lower than the $0.02^\circ 2\theta$ resolution achieved by most laboratory XRD instruments. This results in

broader peaks, increasing detection limits, meaning that crystallite size and strain cannot be fully quantified.

On Earth, phyllosilicates in natural materials are identified after separating particular size fractions (often $<2\ \mu\text{m}$ or smaller) of sediments and soils, followed by a variety of treatments to enhance diffraction intensity and change their basal spacing (e.g., on oriented mounts with glycolation). On Mars, these sample preparations cannot be performed, so it is difficult to distinguish collapsed smectite from illite, for example, because both have $d(001)$ at $10\ \text{\AA}$. Collapsed smectite has lost most interlayer H_2O because of low humidity conditions and is expected within the CheMin instrument [10,23,99], but retains the properties of smectites, namely moderate layer-charge and turbostratic stacking disorder. Illite has an equivalent $d(001)$ peak position but has a higher layer-charge, K^+ fixed in the interlayer, and exhibits ordered layer stacking arrangements. To complicate matters, some phyllosilicates have similar XRD patterns or overlapping peaks and/or EGA- H_2O traces, making it difficult to fully characterize structure and composition.

CheMin and SAM instruments contain a limited number of sample cells and cups to perform analyses and drill campaigns are time consuming (Figure 6). Therefore, sample selection is also limited and carefully considered by the entire MSL team as well as instrument teams. Though sampling is methodically conducted every $\sim 25\text{--}75\ \text{m}$ in vertical topography, it is fragmented. ChemCam and APXS supplement definitive mineralogical X-ray diffraction analyses by providing elemental and chemical trends at a higher resolution. Furthermore, elemental changes are less dramatic than mineralogical changes seen by CheMin, indicating CheMin analyses are crucial to fully characterizing changes in environment and parent material.

5. Review of Phyllosilicate Detections by Curiosity

5.1. Phyllosilicate Results Grouped by Stratigraphy

Through sol 3064, *Curiosity* has drilled 30 samples (Table 1 and Figure 8), and here we review the in-situ phyllosilicate CheMin results by stratigraphic member (Figures 5 and A1). SAM has analyzed 28 sample sites, with multiple drill samples from a single site to obtain the necessary volume of material needed to conduct multiple kinds of analyses. We use the SAM H_2O EGA (Figure 6) data to help determine the species of phyllosilicates present. ChemCam does not detect phyllosilicates directly. Instead, it traces specific elements, such as Li and K, over the rover's traverse. In order to trace the phyllosilicate content within the geological targets analyzed by ChemCam, previous studies have used the Li and H abundances of ChemCam elemental data alongside major element oxides (SiO_2 , TiO_2 , Al_2O_3 , FeO , MgO , CaO , Na_2O , and K_2O) to infer mineralogical variation and calculate weathering indices [87–95]. Our descriptions start at the base of the stratigraphic section (i.e., the oldest rocks) and work up to report on phyllosilicate structures and compositions changing through time (Figures 5 and A1).

Table 1. Comprehensive table of drilled and scooped samples analyzed by CheMin.

Sample Name	Group	Formation	Member	Depositional Environment	Elevation (m)	Drill Sol	Clay (wt. %)	Clay Type	d(001)/ d(021)
Rocknest ^{*1}	n/a	n/a	n/a	Modern aeolian/Recently inactive	−4516.9	61, 66, 69, 74	0	n/a	n/a
John Klein ²	Bradbury	YKB	Sheepbed	Fluvio-Lacustrine	−4519.5	182	22	trioctahedral	~10Å/4.5Å
Cumberland ²	Bradbury	YKB	Sheepbed	Fluvio-Lacustrine	−4519.5	279	18	trioctahedral	~13.2Å/4.5Å
Windjana ³	Bradbury	Kimberley	Dillinger	Reworked aeolian/ fluvial	−4481.5	621	10	trioctahedral	~10Å/4.5Å
Confidence Hills ⁴	Mount Sharp	Murray	Pahrump Hills	Fluvio-Lacustrine	−4460.3	759	8	trioctahedral	~10Å/4.5Å
Mojave 2 ⁴	Mount Sharp	Murray	Pahrump Hills	Fluvio-Lacustrine	−4459.4	882	5	diocahedral	~10Å/4.5Å
Telegraph Peak ⁴	Mount Sharp	Murray	Pahrump Hills	Fluvio-Lacustrine	−4453.2	908	0	n/a	n/a
Buckskin ⁵	Mount Sharp	Murray	Pahrump Hills	Fluvio-Lacustrine	−4446.8	1060	0	n/a	n/a
Big Sky ^{6,7,9}	Siccar Point	Stimson	n/a	Ancient aeolian	−4434.7	1119	0	n/a	n/a
Greenhorn ⁹	Siccar Point	Stimson	n/a	Ancient aeolian	−4434.5	1137	0	n/a	n/a
Gobabeb ^{**}	n/a	n/a	n/a	Modern/ Active aeolian	−4423.8	1224	0	n/a	n/a
Lubango ⁹	Siccar Point	Stimson	n/a	Ancient aeolian	−4429	1320	0	n/a	n/a
Okoruso ⁹	Siccar Point	Stimson	n/a	Ancient aeolian	−4429.3	1332	0	n/a	n/a
Oudam ^{6,7}	Mount Sharp	Murray	Hartmann's Valley	Reworked aeolian/ fluvial	−4435.5	1361	3	Ferri-pyrophyllite	~9.6Å/4.5Å
Marimba ^{6,7}	Mount Sharp	Murray	Karasburg	Fluvio-Lacustrine	−4410.4	1422	28	trioctahedral/ diocahedral	~10Å/4.5Å
Quela ^{6,7}	Mount Sharp	Murray	Karasburg	Fluvio-Lacustrine	−4379.7	1464	16	trioctahedral/ diocahedral	~10Å/4.5Å
Sebina ^{6,7}	Mount Sharp	Murray	Sutton Island	Fluvio-Lacustrine	−4360.8	1495	19	trioctahedral/ diocahedral	~10Å/4.5Å
Ogunquit Beach ^{*** 10}	n/a	n/a	n/a	Modern aeolian	−4300	1651	0	n/a	n/a
Duluth ⁸	Mount Sharp	Murray	Blunts Point	Fluvio-Lacustrine	−4192.5	2057	15	diocahedral	~10Å/4.5Å
Stoer ⁸ (VRR)	Mount Sharp	Murray	Pettegrove Point	Fluvio-Lacustrine	−4169.9	2136	10	diocahedral	~10Å/4.5Å
Highfield ⁸ (VRR)	Mount Sharp	Murray	Jura	Fluvio-Lacustrine	−4147	2224	5	diocahedral	~9.6Å/4.5Å
Rockhall ⁸ (VRR)	Mount Sharp	Murray	Jura	Fluvio-Lacustrine	−4143.8	2261	13	diocahedral	~9.6Å/4.5Å
Aberlady ¹¹ (GT)	Mount Sharp	Murray	Jura	Fluvio-Lacustrine	−4157.94	2370	28	diocahedral	~9.22Å/ ~10Å/4.5Å

Table 1. Cont.

Sample Name	Group	Formation	Member	Depositional Environment	Elevation (m)	Drill Sol	Clay (wt. %)	Clay Type	d(001)/ d(021)
Kilmarie ¹¹ (GT)	Mount Sharp	Murray	Jura	Fluvio-Lacustrine	−4157.95	2384	28	dioctahedral	~9.22Å / ~10Å / 4.5Å
Glen Etive ¹¹ (GT)	Mount Sharp	Murray	Knockfarril Hill	Fluvio-Lacustrine	−4133.36	2486	34	dioctahedral	~10Å / 4.5Å
Glen Etive 2 ¹¹ (GT)	Mount Sharp	Murray	Knockfarril Hill	Fluvio-Lacustrine	−4129.62	2527	26	dioctahedral	~10Å / 4.5Å
Hutton ¹²	Mount Sharp	Murray	Glasgow	Fluvio-Lacustrine	−4095.37	2668	6.3	dioctahedral	~10Å / 4.5Å
Edinburgh ^A	Siccar Point	Stimson	n/a	Ancient aeolian	−4088.69	2711	7	dioctahedral	~10Å / 4.5Å / Future publication
Glasgow ^A	Mount Sharp	Murray	Glasgow	Fluvio-Lacustrine	−4107.93	2754	24	dioctahedral	~10Å / 4.5Å / Future publication
Mary Anning ¹²	Mount Sharp	Murray	Knockfarril Hill	Fluvio-Lacustrine	−4128.06	2839	28	dioctahedral	~10Å / 4.5Å
Mary Anning ^{3 12}	Mount Sharp	Murray	Knockfarril Hill	Fluvio-Lacustrine	−4128.06	2872	30	dioctahedral	~10Å / 4.5Å
Groken ¹²	Mount Sharp	Murray	Knockfarril Hill	Fluvio-Lacustrine	−4127.91	2914	Future publication	dioctahedral	~9.22Å / ~10Å / 4.5Å
Nontron	Mount Sharp	Murray	Glasgow	Fluvio-Lacustrine	−4066.51	3064	Future publication	Future publication	Future publication

* Near landing site. ** Bagnold dune field/namib dune. *** Bagnold dune field/mount desert island. ¹ from [100], ² from [10], ³ from [101], ⁴ from [102], ⁵ from [103], ⁶ from [11], ⁷ from [98], ⁸ from [104], ⁹ from [105], ¹⁰ from [106], ¹¹ from [107], ¹² from [12], ^A Data available in nasas planetary data system (<https://pds.nasa.gov/>), accessed on 23 July 2021.

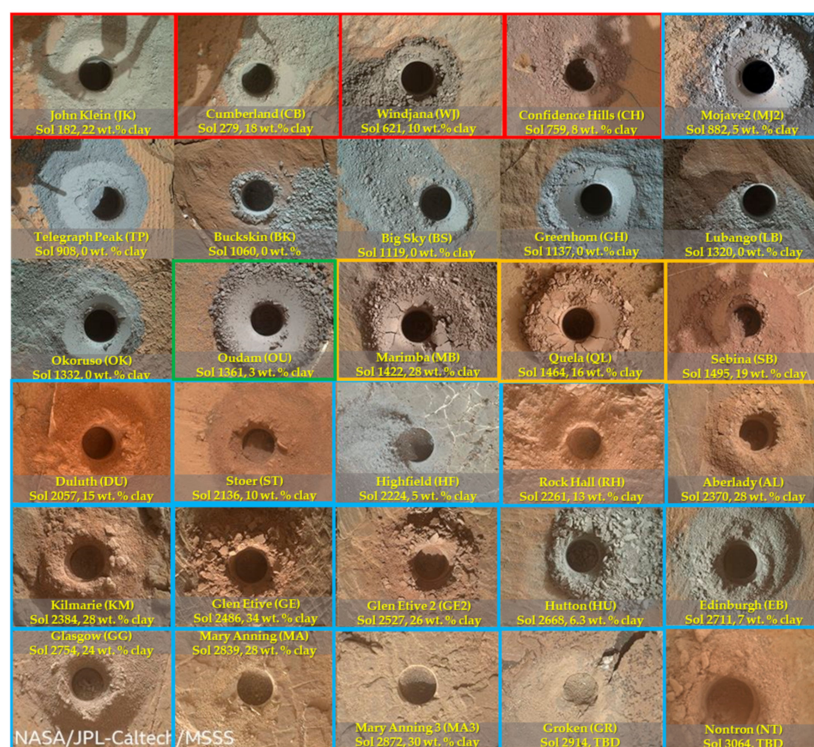


Figure 8. Gale crater drill hole sites imaged by MAHLI (30). Drill holes are approximately 1.5 cm in diameter and reach a depth of up to ~4–6 cm. Trioctahedral clay samples are outlined in red, dioctahedral in blue, both tri- and dioctahedral in orange, and ferripyrophyllite in green. Drilled powered samples exhibit a range of grey and reddish colors that reflect mineralogical changes from alteration and fluid:rock interactions.

5.1.1. Yellowknife Bay and Kimberly Formations in the Bradbury Group

The Bradbury group consists of deposits on the northwestern plains of Gale crater. The rocks of the Bradbury group include mudstone, sandstone, and conglomerate, which were deposited in lacustrine and fluvio-deltaic environments [4,49]. Three rock samples were drilled from the Bradbury group: two from mudstone in the Yellowknife Bay formation and one from sandstone in the overlying Kimberly formation (Figures 5 and A1).

Sheepbed Member (John Klein (JK), Cumberland (CB), Windjana (WJ)): *Curiosity* drilled its first rock samples at Yellowknife Bay (YKB), located east of *Curiosity's* landing site (Figure 9). YKB is interpreted to be the site of an ancient lake [4] and is the lowest part of the crater that *Curiosity* studied. The rocks represent the oldest deposits that *Curiosity* has investigated to date [5]. The two samples drilled in the Sheepbed mudstone are named “John Klein” (JK) and “Cumberland”(CB), which were drilled a few meters apart to investigate changes in mineralogy and geochemistry and assess evidence for early-stage diagenesis [4,108–110]. JK and CB contain ~18–22 wt.% trioctahedral smectite [10,23,111] (Table 1, Figures 5, 9 and 10). The JK sample exhibits a basal peak with a d-spacing of ~10 Å characteristic of collapsed, dehydrated smectite and the CB sample has more complex basal peak with contributions at ~10 Å and ~13.2 Å [10,23] (Figures 9 and 10). The “Windjana” (WJ) sample is the sole sample collected from the Kimberly formation, in the Dillinger member (Figures 5 and A1). WJ was drilled from reworked deltaic and aeolian sediments [54] derived from a diverse set of volcanic sources, evident in an enrichment in alkali feldspar (var. sanidine) and pyroxene and the presence of plagioclase feldspar [101]. The WJ CheMin XRD pattern has a weak d(001) peak at 10 Å and an d(021) peak at 4.5 Å (Figure 10). Based on CheMin and SAM data, the sample contains 10 wt. % trioctahedral phyllosilicate (Table 1 and Figure 11) [78,80,112]. All samples in the YKB and Kimberly formations evolved water during SAM-EGA analyses. The water evolved between 100 °C and

300 °C is likely from H₂O in smectite interlayers in CB, JK, and WJ [80], and water evolved between 650 °C and 800 °C is likely from the dehydroxylation of phyllosilicates [112] (Figure 11).

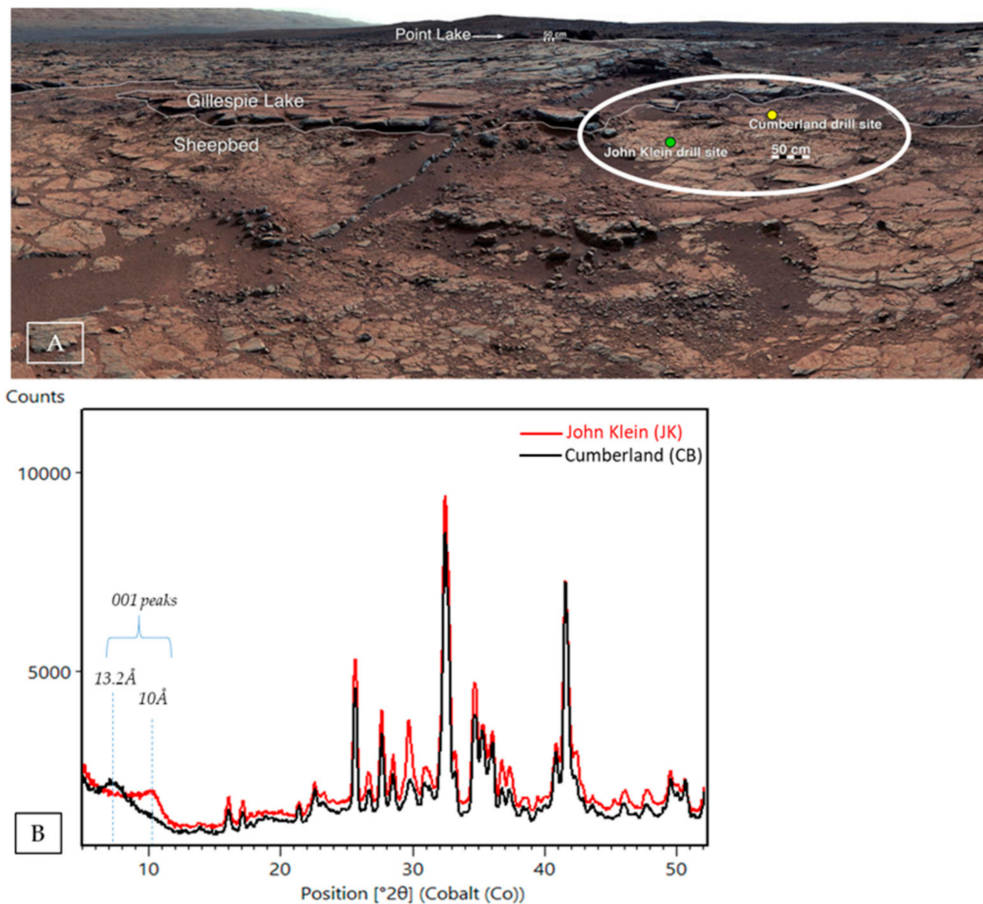


Figure 9. (A) Mastcam mosaic of Yellowknife Bay showing the drill sites of John Klein and Cumberland. (B) CheMin X-ray diffraction patterns of the Cumberland (black) with a basal 001 d-spacing of 13.2 Å and John Klein (red) drill samples, with a basal 001 d-spacing of 10 Å.

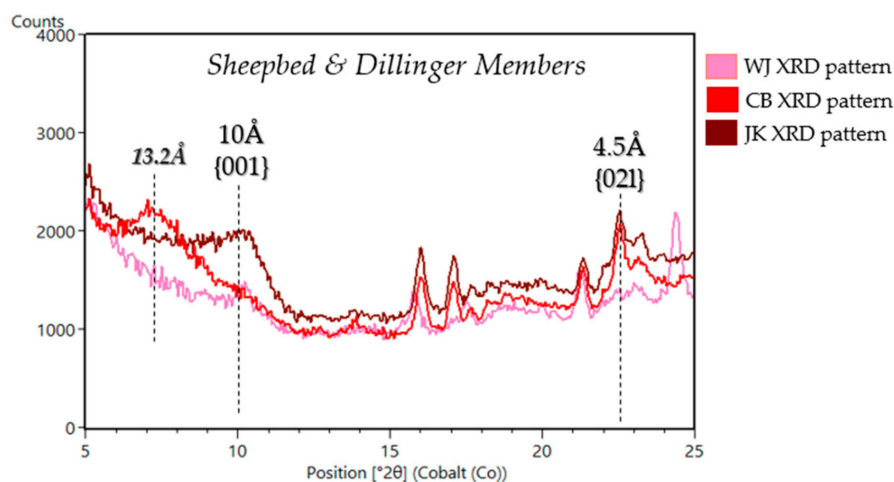


Figure 10. CheMin XRD patterns from 5° to 25° 2θ of drill samples from the Bradbury group. The d(001) and d(021) peaks are denoted by dashed black lines. A pronounced 10 Å d(001) peak is seen in the JK pattern and an uncharacteristic 13.2 Å peak is observed in the CB pattern, signifying potential partial chloritization (i.e., pillaring) of the smectite structure.

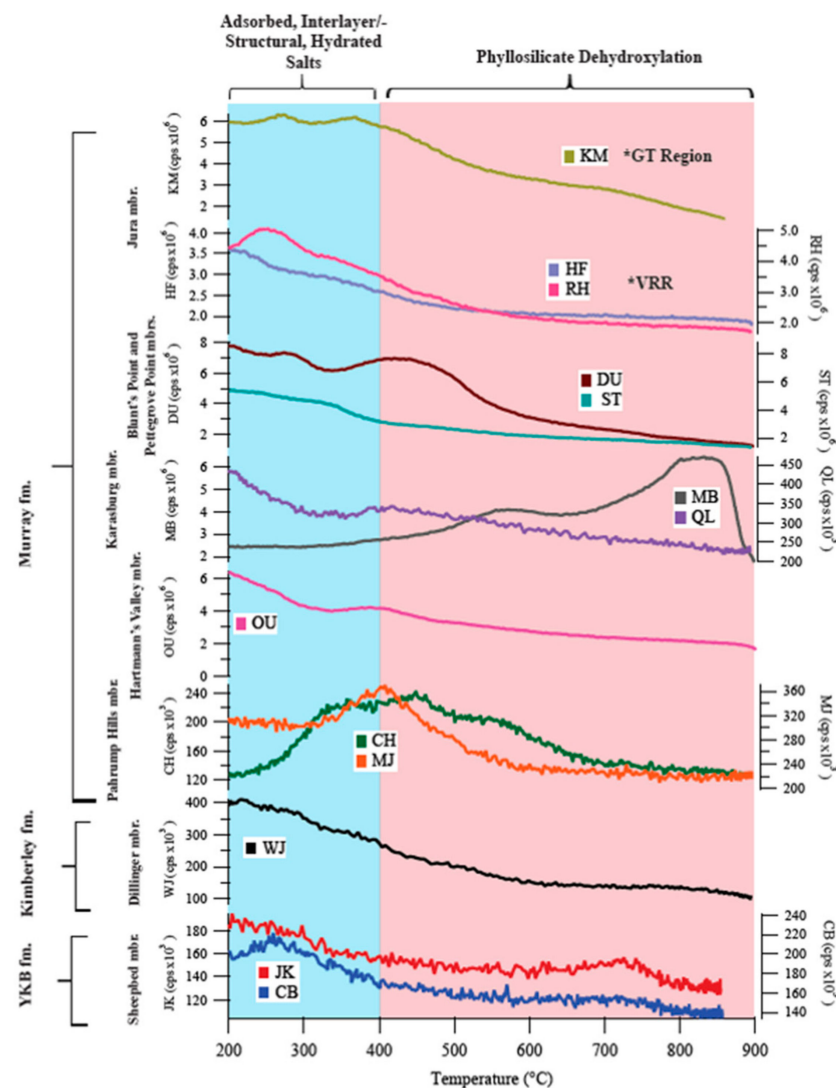


Figure 11. SAM H₂O EGA results for samples grouped by stratigraphic members. The dehydration temperature ranges of H₂O for adsorbed and interlayer water are highlighted in blue, and the dehydroxylation temperature ranges for phyllosilicates are highlighted in red.

5.1.2. Murray Formation in the Mount Sharp Group

The Mount Sharp group comprises the sub-horizontal strata exposed in the foothills of Mount Sharp. The Murray formation is primarily composed of lacustrine mudstones, covers over 370 m of vertical stratigraphy, and includes nine members. The Murray formation also contains the most drilled rock samples analyzed of any formation (24 samples in total to sol 3064). For a more comprehensive review of the sedimentary stratigraphy, refer to [5–9,49–52].

Pahrump Hills Member (Confidence Hills (CH), Telegraph Peak (TP), Buckskin (BK), Mojave2 (MJ)): The Pahrump Hills member consists of laminated lacustrine mudstone with thick (cm-scale) and thin (mm-scale) laminations indicative of shallow and deep lake waters, respectively [5,6,49]. Samples drilled in this member include “Confidence Hills” (CH), “Mojave2” (MJ), “Telegraph Peak” (TP), and “Buckskin” (BK). Out of all of the members in the Murray formation, Pahrump Hills has among the lowest phyllosilicate abundances. Only CH and MJ contain phyllosilicates (8 wt. % and 5 wt. %, respectively) (Table 1, Figures 5 and A1) [102]. The phyllosilicates in CH and MJ appear to be typical collapsed smectite with a basal d(001) of 10 Å (Figure 12) seen elsewhere in the Murray formation. Both CH and MJ have broad, weak d(001) peaks, indicating the smectite is

poorly crystalline [102]. A distinct d(021) peak is absent, making it difficult to identify the type of smectite from CheMin data alone. SAM EGA data, however, are consistent with trioctahedral smectite in CH and dioctahedral smectite in MJ, with H₂O evolved between 650 °C and 800 °C from the dehydroxylation of phyllosilicates consistent with Mg and/or Al in the octahedral sheets of smectite [80,102] (Figure 11). TP and BK, by comparison, do not contain a phyllosilicate signature (Figure 12) [102].

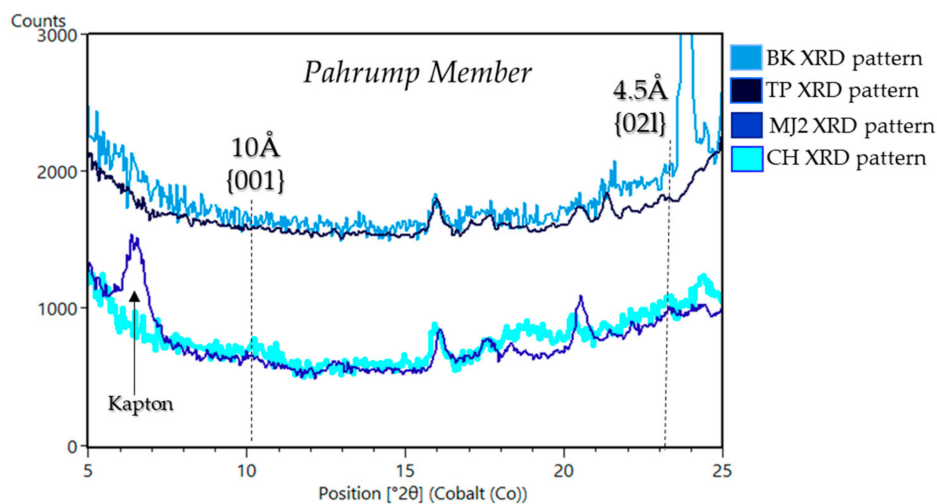


Figure 12. CheMin XRD patterns from 5° to 25° 2θ of samples from the Pahrump Hills member. The basal d-spacing peaks of the d(001) of 10 Å and d(021) of 4.5 Å are denoted by dashed black lines. Broad 10 Å peaks are seen in the CH and MJ2 patterns, in contrast to the lack of d(001) and d(021) peaks in the TP and BK patterns that do not contain phyllosilicates. Kapton peak artifact is part of the sample cell and is not in the rock powders.

Hartmann’s Valley Member (Oudam (OU)): “Oudam” (OU) was sampled from a cross-stratified siltstone to very fine sandstone ~25 m thick that is either aeolian or fluvial in origin [113–115]. Analyses of OU CheMin diffraction data show the sample contains ~3 wt. % phyllosilicate and has an unusual basal d-spacing of ~9.6 Å (Table 1, Figures 5, 13 and A1). This d-spacing could be explained by a smectite that was altered by acidic fluids (e.g., [116]) or by ferripyrophyllite, an Fe³⁺ phyllosilicate in the pyrophyllite-talc group. SAM EGA data are consistent with a Fe³⁺-rich phyllosilicate in OU, with an H₂O release at 470 °C, which fits with the CheMin interpretation of ferripyrophyllite [11,98] (Figure 11).

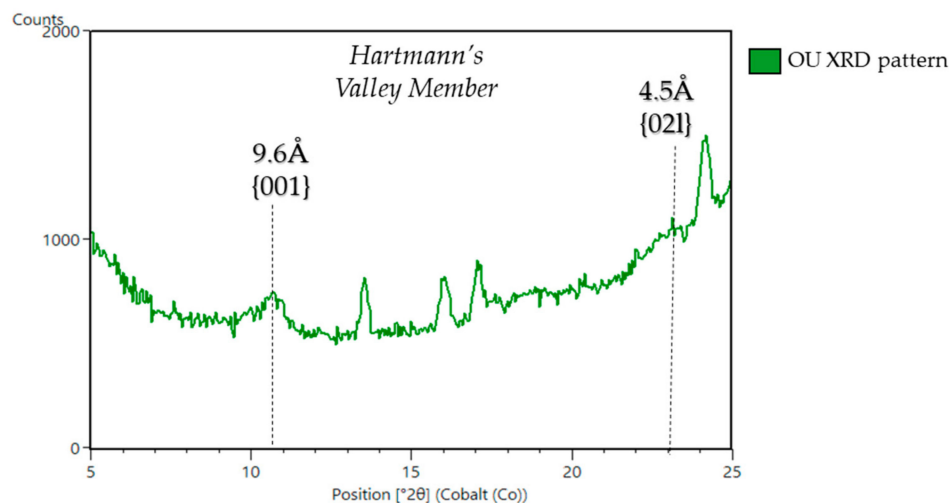


Figure 13. CheMin XRD pattern from 5° to 25° 2θ of the Hartmann’s Valley member drilled sample, OU. The d(001) and d(021) peak positions are identified at 9.6 Å and 4.5 Å, respectively.

Karasburg & Sutton Island Members (Marimba (MB), Quela (QL), Sebina (SB)): Al- and Fe- smectites have been observed using orbital visible and near-infrared (VNIR) spectra in the Karasburg and Sutton Island members of the Murray formation [117,118]. “Marimba” (MB) and “Quela” (QL) were sampled from the Karasburg member from finely laminated mudstones that represent sub-aqueous deposition in a lacustrine environment [11,113–115]. The “Sebina” (SB) sample was drilled from the Sutton Island member, which is comprised of heterolithic mudstone-sandstone and contains desiccation cracks which indicates subaerial exposure at Gale [11,113–115]. Phyllosilicate abundances in these samples range from ~15 wt. % to 28 wt. % and have a basal d(001) of ~10 Å and d(021) of ~4.5 Å, indicating a 2:1 group phyllosilicate [11,98] (Table 1, Figures 5, 14 and A1). The lack of a correlation between APXS-measured potassium and phyllosilicate abundance suggests that the 10 Å phyllosilicate is collapsed smectite, rather than illite [11]. SAM H₂O EGA data show dehydroxylation of phyllosilicates in MB occurred at 610 °C and 825 °C, which is consistent with the presence of both dioctahedral and trioctahedral smectites [98,119–121] (Figure 11). Laboratory EGA of phyllosilicates in a SAM testbed instrument indicate that MB, QL, and SB contain a mixture of Al-rich and Mg-rich smectite.

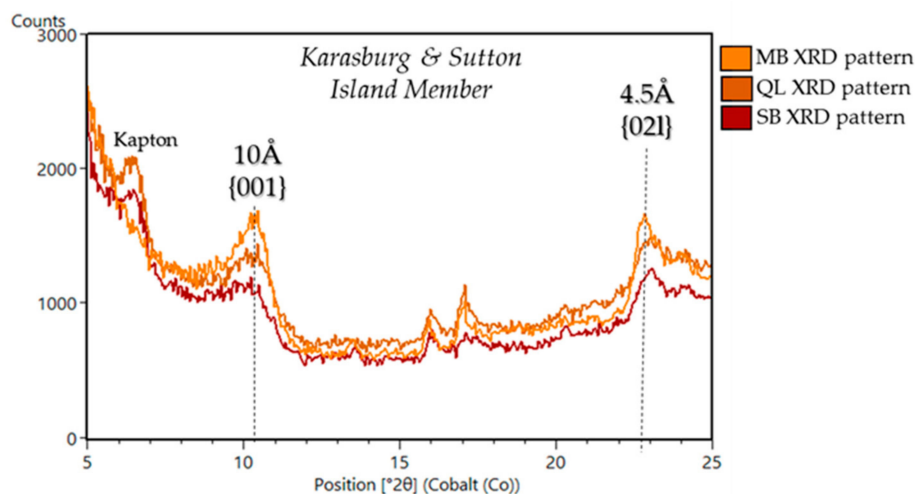


Figure 14. CheMin XRD patterns from 5° to 25° 2θ of samples from the Karasburg and Sutton Island members. The basal d-spacing peaks of the 001 of 10 Å and 021 of 4.5 Å are denoted by dashed black lines. A pronounced 10 Å peak is seen in the MB and QL patterns, some of the highest phyllosilicate abundances are seen at this location. Kapton peak artifact is part of the sample cell and not in the rock powders.

Blunts Point and Pettegrove Point (VRR) Members (Duluth (DU), Stoer (ST)): The single sample drilled in the Blunts Point member, “Duluth” (DU), was drilled just below an indurated ridge, ~6.5 km long and ~200m wide, called Vera Rubin ridge (VRR) (Figure 2b). Blunts Point is made of laminated, fine-grained mudstone cross-cut by abundant, curvilinear Ca-sulfate veins [5,9]. VRR was formerly known as “Hematite Ridge” [122] because orbital CRISM spectra of the ridge have deep absorptions attributed to hematite [3,117,123]. Investigating VRR was part of an MSL mission campaign to determine the unique geological history of the ridge and the processes that led to the formation of hematite and the geomorphic ridge [68,123]. VRR comprises the Pettegrove Point and Jura members, both of which are dominated by finely laminated lacustrine mudstone facies [9] (Figures 5 and A1). The MSL team attempted to drill in rocks with the deepest spectral absorption attributed to hematite but the rover was unable to obtain optimum sampling depth of ~4 cm due to the rock strength [68,124]. The sample “Stoer” (ST) was drilled in the Pettegrove Point member on VRR but did not itself exhibit deep spectral absorptions attributed to hematite [68,124].

DU contains ~15 wt. % phyllosilicate and has an d(001) of ~10 Å and a d(021) of ~4.5 Å, consistent with a collapsed smectite or illite (Table 1, Figures 5, 15 and A1). The low

abundance of K_2O from APXS (0.94 wt. % K_2O [125]), however, suggests collapsed smectite is present rather than illite (e.g., [11]) because the observed K_2O in DU is accounted for by other K-bearing minerals in the sample such as sanidine. SAM EGA data indicate the presence of nontronite in DU based on the H_2O release temperature [126] (Figure 11), which is also supported by BGMN models of CheMin data. DU was the first fully dioctahedral smectite detected by *Curiosity* [122]. ST contains ~10 wt. % phyllosilicate, with a $d(001)$ at 9.6 Å, but the $d(021)$ peak was too weak to determine the b-unit cell [122] (Table 1, Figure 15). SAM-EGA data from ST show H_2O evolved between 350 °C and 600 °C indicating a very Fe^{3+} -rich dioctahedral phyllosilicate [126] (Figure 11). Like the 9.6 Å phyllosilicate in Oudam, the $d(001)$ at 9.6 Å could be from smectite altered by acidic fluid, causing further collapse of the structure beyond dehydration or from ferripyrophyllite [122].

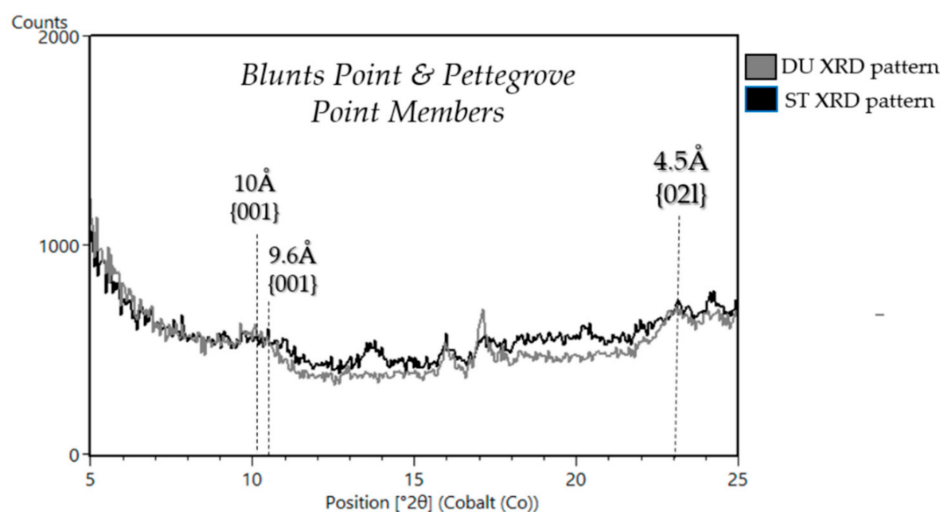


Figure 15. CheMin XRD patterns from 5° to 25° 2θ of samples from the Blunts Point member (DU) and the Pettegrove Point member (ST). The position of the $d(001)$ and $d(021)$ peaks are denoted by dashed black lines.

Jura Member (HF(VRR), RH (VRR), AL (GT), KM (GT)): The Jura member consists of laminated mudstone and outcrops at the top of VRR and the base of GT. The Jura on VRR is heterogeneous in color and displays tones of red, purple, and grey [127] (Figure 2b). Two samples were drilled in the Jura member exposed on VRR. The sample “Highfield” (HF) was drilled from the gray-toned Jura and “Rock Hall” (RH) was drilled in the red-toned Jura, [122]. HF contains ~5 wt. % phyllosilicate and RH contains ~13 wt. % (Table 1, Figures 5 and A1). The $d(001)$ of the phyllosilicates in HF and RH are ~9.6 Å, like in ST and OU, consistent with ferripyrophyllite [122] (Figure 16). The RH sample is also consistent with dioctahedral occupancy, similar to samples in the Blunts Point and Pettegrove Point members, however HF yielded a low phyllosilicate abundance with only a small $d(021)$ peak compared to other VRR samples [122] (Figure 16). HF $d(021)$ peak, similar to ST, lacked a pronounced $d(021)$ peak, making it possible to perform BGMN modeling and determine the b-unit cell length [122]. EGA data from HF and RH support the identification of Fe-rich dioctahedral 2:1 phyllosilicate, based on the H_2O evolved between 350 °C and 600 °C [122] (Figure 11).

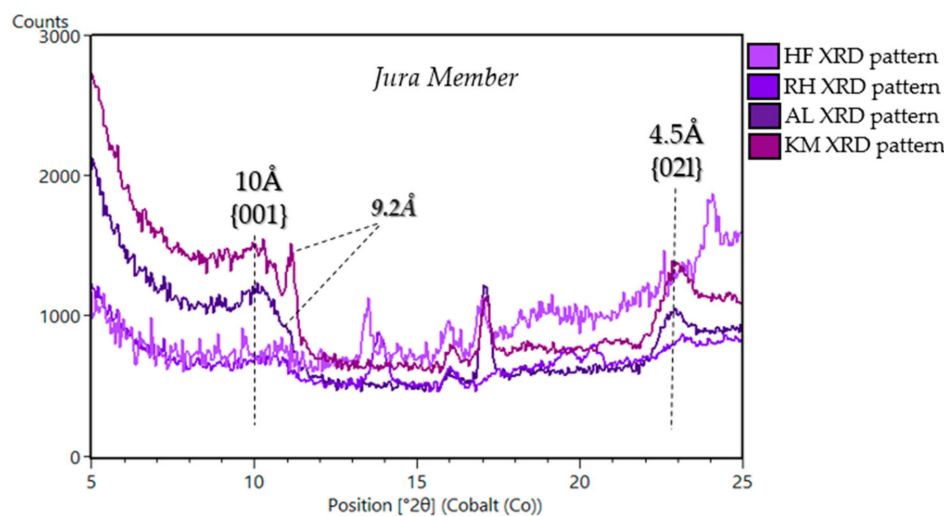


Figure 16. CheMin XRD patterns from 5° to 25° 2θ of samples from the Jura member (VRR—HF and RH, and GT—AL and KM). The position of the d(001) and d(021) peaks are denoted by dashed black lines.

GT is a region to the south of VRR, defined by a shallow trough that strikes W-E and is up to ~0.3–1 km wide to the north of VRR [107] (Figure 2b). Strata within GT exhibit strong spectral absorptions attributed to Fe/Mg-smectites in orbital VSWIR spectra [1,3,117,128] (Figure 4). Outcrops contain thinly/thickly laminated mudstones and can exhibit fracture, rubbly, and alternating recessive and resistant laminations [107]. Two samples were drilled from thinly laminated mudstone in the Jura member of GT, “Aberlady” (AL) and “Kilmarie” (KM). AL and KM exhibit d(001) peaks at ~9.22 Å and ~10 Å, and consist of ~28 wt. % phyllosilicate [107] (Table 1, Figures 5, 16 and A1). The d(001) peak is consistent with collapsed smectite, but the 9.2 Å could be from a number of minerals, including phyllosilicates, zeolites, rhomboclase, and jahnsite-whiteite. APXS data were used in conjunction with CheMin data to help identify the ~9.2 Å phase present in these samples, and a favored interpretation is that the 9.2 Å peak is the basal spacing of a mixed-layer talc/serpentine [107]. SAM did not analyze AL, but SAM-EGA data from KM yield H₂O release temperatures of ~400–600 °C (Figure 11), consistent with the dehydroxylation of an Fe³⁺-rich dioctahedral smectite [107]. SAM EGA data also indicate an H₂O release at ~715 °C that was not related to the Fe-smectite in KM [107] (Figure 11).

Knockfarril Hill Member (GE, GE2, MA, MA3, GR): CheMin analyzed five samples from the Knockfarril Hill member in GT: “Glen Etive” (GE), “Glen Etive 2” (GE2), “Mary Anning” (MA), “Mary Anning 3” (MA3) and “Groken” (GR). The Knockfarril Hill member consists of cross-stratified sandstones [107] and contains the most phyllosilicate-rich samples analyzed to date by CheMin [12]. GE and GE2 were drilled from the same outcrop, and MA, MA3, and GR were drilled from the same outcrop. The MA/MA3/GR outcrop was specifically targeted to be at the same elevation as GE/GE2 to select a phyllosilicate-rich outcrop for SAM wet chemistry experiments. GE and GE2 contain the highest phyllosilicate abundances (28–34 wt. %) in the bulk rock (Table 1, Figures 5 and A1) [107]. A d(001) at ~10 Å and d(021) at ~4.5 Å is observed in all samples from the Knockfarril Hill member, suggesting a collapsed smectite (Figure 17) [107]. The MA3 and GR patterns also shows a ~9.22 Å peak, similar to the peak observed in AL and KM [12] (Figure 17). The detailed phyllosilicate mineralogy of MA, MA3, and GR will be the topic of upcoming publications.

Glasgow member (GG, HU): CheMin analyzed 2 samples from the Glasgow member: “Hutton” (HU) and “Glasgow” (GG) (Figures 5 and 18). The Glasgow member contains finely laminated, light-toned, highly fractured bedrock [129] and this member, at the time of writing, is currently being assessed by the MSL team and will be the subject of an upcoming in-depth discussion in a future publication.

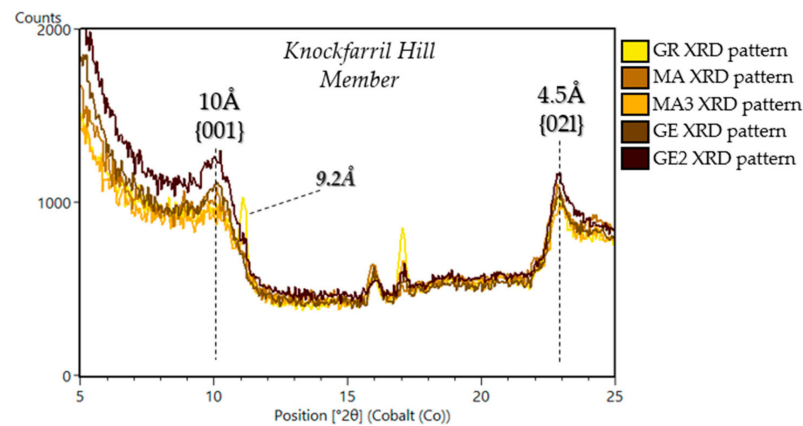


Figure 17. CheMin XRD patterns of samples from the Knockfarril Hill member. The position of the $d(001)$ and $d(021)$ peaks are denoted by dashed black lines. A pronounced 10 \AA peak is seen in the all patterns and peaks at $\sim 9.22 \text{ \AA}$ and 11.1 \AA are observed in the GR pattern, and the GR sample is the topic of an upcoming special edition publication on GT.

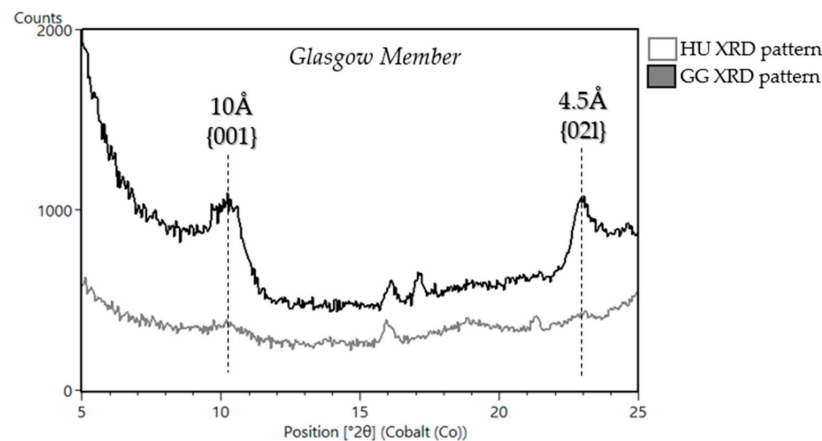


Figure 18. CheMin XRD patterns of the Glasgow member. The basal d -spacing peaks of the 001 of 10 \AA and 021 of 4.5 \AA are denoted by dashed black lines. A pronounced 10 \AA peak is seen in the GG pattern and these samples are a topic of discussion of an upcoming publication.

5.1.3. Stimson Formation in the Siccar Point Group (Big Sky (BS), Greenhorn (GH), Lubango (LB), Okoruso (OK), Edinburgh (EB))

The Stimson formation represents the youngest rocks studied by *Curiosity*, and is part of the Siccar Point group, which consists of an ancient lithified aeolian dune field [53,117] and unconformably overlies the Mount Sharp group. This unconformity resulted from cessation of sediment deposition, and subsequent removal of a significant portion of the Bradbury and Murray rocks, and represents a major change in the climate and depositional regime [53]. The transition from lacustrine mudstones to aeolian sandstones is not well-persevered and therefore there is a time gap between these formations as evident by the clasts of Murray formation that are reworked at the base of the Stimson [53,130]. Outcrops of the Stimson formation were investigated by *Curiosity* at the Naukluft and Emerson plateaus near the base of the Murray formation after the Pahrump Hills campaign and again recently on the Greenhough pediment during the GT campaign. The Stimson at the Naukluft and Emerson plateaus shows evidence for late diagenesis in the form of bright-toned, fracture-associated halos. Samples that were measured in the Stimson formation include two samples that were drilled in alteration halos “Greenhorn” (GH) and “Lubango” (LB) and two samples that were drilled in the parent sandstone in close proximity for comparison “Big Sky” (BS) and “Okoruso” (OK) [105]. CheMin did not detect phyllosilicates in samples from the Naukluft and Emerson plateaus (Table 1, Figures 5, 19

and A1). Water released at 500 °C from SAM EGA of Stimson materials could be associated with hydroxylated amorphous Al/Si phases or water trapped within amorphous phases, and not attributed to phyllosilicates [80] (Figure 11).

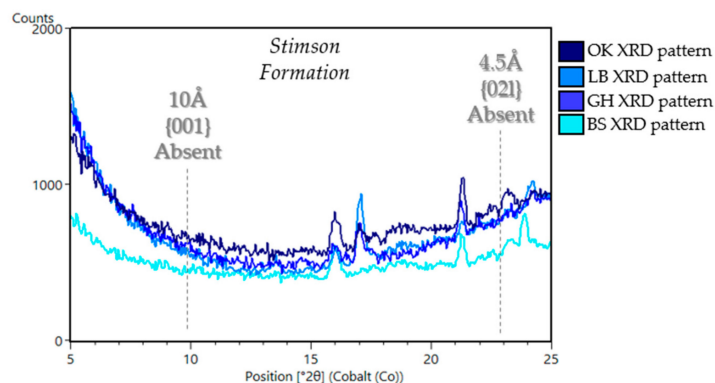


Figure 19. CheMin XRD patterns from 5° to 25° 2θ of samples from the Stimson formation. The basal d-spacing peaks of the d(001) and d(021) are absent in the Stimson samples, which indicates the absence of phyllosilicates in these samples.

The sample “Edinburgh” (EB) was drilled in the Greenheugh pediment capping unit, which is considered an up-slope extension of the Stimson formation and part of the Siccar Point group [53,130–132]. The CheMin XRD pattern of EB shows an (021) peak at ~4.5 Å and an especially weak, broad peak at 10 Å, consistent with a poorly crystalline collapsed smectite (Figure 20). The detailed clay mineralogy of EB, including the SAM EGA data, will be reported in a future publication. For a more comprehensive sedimentary stratigraphy review of the Stimson formation, refer to [53].

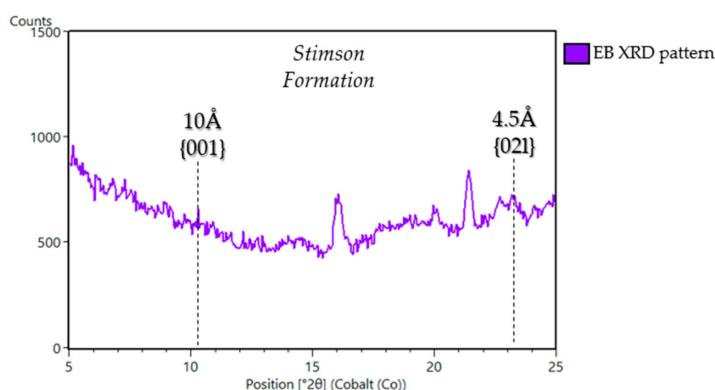


Figure 20. CheMin XRD pattern from 5° to 25° 2θ of sample EB. The basal d-spacing peaks of the 001 of 10 Å and 021 of 4.5 Å are denoted by dashed black lines. A weak, broad 10 Å peak is seen in the EB indicating a poorly crystalline phyllosilicate.

6. Discussion and Interpretations

It is through the unique instrument combination of CheMin XRD, SAM EGA, APXS, and ChemCam that phyllosilicates can be characterized and distinguished in situ on Mars. In situ phyllosilicates are identified in CheMin XRD data by observing d(001) and d(021) peak locations (Figure 7), which are a measure of the interplanar spacing along the c- and b-axes, respectively. SAM EGA data further constrain the identification of phyllosilicate species by measuring the temperature of H₂O release from the dehydroxylation of octahedral sheets, which is characteristic of specific phyllosilicates. APXS and ChemCam also support the detection of phyllosilicates by measuring and assessing chemical trends in elements common in phyllosilicates, such as K and Li [87], and potentially B [133]. Data from these instrument suites led to the identification of phyllosilicates in nearly every

ancient fluvio-lacustrine sample analyzed by CheMin. Furthermore, the data from *Curiosity* suggest phyllosilicate diversity exists in Gale crater that was not appreciated from orbital data alone. Most clays detected by *Curiosity* are collapsed smectite, but we see some important changes in phyllosilicate structure and composition within the stratigraphy that signify changes in source and/or alteration environment [10,11,23,102,107,134]. This diversity points towards a variety of aqueous environments in the ancient Gale crater, particularly groundwater–sediment interactions during burial diagenesis, and provides clues concerning habitability.

6.1. Smectitic Samples in Gale Crater

Almost all of the phyllosilicates detected by CheMin have a $d(001)$ of ~ 10 Å, which is consistent with illite or a collapsed (i.e., dehydrated) swelling phyllosilicates such as smectite [67]. The lack of a correlation between phyllosilicate abundance and K_2O content from APXS, however, suggests the 10 Å phase in CheMin patterns is collapsed smectite, rather than illite [11], and therefore sediments did not reach the smectite-illite transition. Orbital spectral data suggest that smectites at the Martian surface are dehydrated, and these in situ measurements likely confirm this hypothesis [22,67,135] however the relative humidity inside CheMin is lower than the Martian surface [23] and therefore some uncertainty remains. The highest smectite abundances are observed in Murray formation fluvio-lacustrine samples: GE (34 wt. %), KM, AB, MB (28 wt. % each), and GE2 (26 wt. %). With the exception of MB, these samples with abundant smectite were drilled from GT, which has a strong signature of Fe/Mg-smectite from orbit, providing a ground-truth to orbital observations made by CRISM (Figure 4). It is important to note that CheMin detected phyllosilicates in locations that did not have a phyllosilicate signature in CRISM spectra, demonstrating the importance of in situ mineralogical investigations for identifying the mineral assemblages and from those characterizing aqueous environments on Mars.

Monitoring changes in mineralogy along *Curiosity*'s traverse is key to understanding fluctuations in potential habitability and the depositional environment, and their implications of the aqueous history of Gale crater. Smectites in Gale crater record a transition to a more oxidative, open system alteration in response to the lake drying out periodically, as indicated in a shift from trioctahedral to dioctahedral smectites traversing up-section [11,23]. Trioctahedral smectites tend to form first during the alteration of olivine and are subsequently replaced by dioctahedral minerals. During this alteration process, Fe^{2+} and Mg^{2+} are leached, Fe^{2+} is oxidized, and passive enrichment of Si and Al occurs, leading to the formation of an Al-bearing dioctahedral smectite, though trioctahedral smectite can also be Fe^{3+} -rich [11,29,30,33].

Although the initial detection of smectite on the Martian surface from orbit led to the hypothesis that alkaline fluids were prevalent on early Mars (e.g., [136]), smectite can form at a variety of pH, including acidic and circum-neutral pH conditions [137–142]. Nontronite, montmorillonite, and saponite are typically formed in acidic to circum-neutral pH conditions [143–147]. Trioctahedral smectite found at the base of the section, along with the presence of magnetite, may indicate formation from low-salinity pore waters in circum-neutral pH (7.8–8.6) [10,23,94,148]. The $d(02l)$ peak in CheMin patterns from ancient fluvio-lacustrine samples shifts to the right (i.e., to smaller d -spacing) going up-section, indicating that the smectites transitioned from trioctahedral to dioctahedral within the section (Figure 21). Dioctahedral smectites commonly form from aqueous alteration in open systems [139,140]. The shift from trioctahedral to dioctahedral going up-section and the disappearance of abundant magnetite at the base of the section at the expense of hematite up-section, suggests the ancient lake waters or diagenetic fluids were more oxidative up-section (Figures 5 and A1). Furthermore, episodic lake drying, as evidenced from the preserved desiccation cracks [51], and chemical indicators of open-system weathering [89] may have produced Al-rich, Fe-bearing dioctahedral smectite via near-surface chemical weathering as a result of fluctuations in lake level and atmospheric infiltration [11,134]. Additionally, the lowest strata in Gale crater, at YKB, which would have experienced the

highest temperatures due to a lack of overburden evidence of chloritization of trioctahedral smectites, readily detectable with CheMin [10,23]. This and the absence of evidence for a pronounced smectite-illite transition in Gale samples is noteworthy, suggesting an absence of significant burial diagenesis.

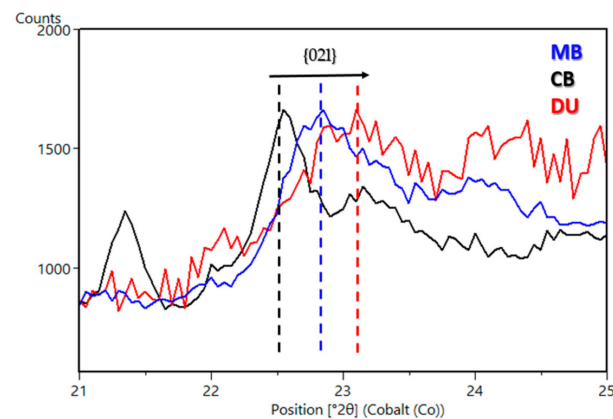


Figure 21. XRD patterns from 20–25° 2θ of the samples CB, MB, and DU to show the position of the d(021) peaks. The XRD patterns of these samples demonstrate a shift from trioctahedral smectite in CB to mixed trioctahedral-dioctahedral smectite in MB to a fully dioctahedral smectite in DU. These shifts in the d(021) peak represent environmental changes that are reflected in the phyllosilicates present in Gale crater.

6.2. Non-Smectitic Phyllosilicate Samples in Gale Crater

The majority of phyllosilicates in Gale crater are smectites with a collapsed basal spacing of 10 Å. However, phyllosilicates that deviate from the predominant basal spacing of 10 Å have been observed. Although we primarily see collapsed smectite, there is evidence for expanded smectite in YKB. It has been hypothesized the ~13.2 Å basal spacing for the sample CB is caused by low temperature Mg-rich diagenetic fluids that partially chloritize the smectite by precipitating domains of Mg-OH in the interlayer sites to keep the structure propped open (Figure 3) [10,23]. A peak with a basal spacing of ~9.6 Å is present in the samples OU, HF, and RH, and this may be the basal peak of ferripyrophyllite, which is a ferric phyllosilicate in the talc-pyrophyllite group that commonly forms in warm, saline fluids. Alternatively, smectites altered by acidic fluids can collapse below 10 Å to explain the 9.6 Å peak [11,98,104,116]. Mixed-layer nontronite-talc was also considered as a possible explanation for the 9.6 Å basal peak [122]. However, SAM EGA data do not support the presence of talc due to the lack of a high-temperature H₂O evolution [126]. A sharp peak at 9.2 Å is present in the samples KM and GR, which is hypothesized to be the basal peak of a mixed-layer serpentine/talc (S-T). If present, serpentine/talc would likely be detrital and indicative of hydrothermalism of ultramafic volcanic rocks (serpentinization) in the sediment source region rather than in situ because the mineral assemblage does not contain other high-temperature phases [107].

6.3. Phyllosilicates, Formation and Organic Preservation

Martian phyllosilicates are important for understanding the fluid–rock interactions, aqueous conditions and durations present in Gale crater. Previously, Martian phyllosilicates were hypothesized to be detrital in nature and sourced from subsurface processes of Noachian age [34,35]. However, phyllosilicates present in Gale crater demonstrate that Martian clay minerals formed in situ via near-surface processes altering basaltic sediments that this occurred long after the Noachian into the Hesperian [10,11,149]. These in-situ phyllosilicates are significant to Gale crater because they provide important constraints on the habitability of ancient Martian environments [4,10,11,23,63,67]. Evidence for in-situ phyllosilicate formation during or close to the time of deposition includes the bulk

chemistry of the mudstones being similar to the average Martian basalt [10,94], and the fact that phyllosilicates are monomineralic, unlike detrital phyllosilicates that may contain various types of phyllosilicate minerals created by weathering profiles or hydrothermally altered crust [11,23]. Additional evidence is derived from the mass balance calculations afforded by the quantitative mineralogy of the reactants versus products [11], and the fact that changes in lake conditions inferred from bulk geochemistry and sedimentology are reflected in the changes observed in smectite chemistry going up-section [23]. Diagenesis that occurred thousands of years after deposition has also been proposed as a phyllosilicate formation mechanism in the YKB formation [149]. However, terrestrial phyllosilicate production and smectite formation have been reported to occur on a much shorter time scale (i.e., weeks to years) in marine and mangrove swamp sediments [150,151].

Organic carbon has been discovered in ~3.5-billion-year-old lacustrine mudstone in Gale crater, as measured by the SAM instrument suite onboard *Curiosity* [15,16]. Understanding the potential of phyllosilicates to preserve organics is key to understanding habitability in Gale crater as organic detections add to the pool of available energy and carbon sources of the past environment, and organics may offer clues to their formation, concentration, and subsequent processing within the geologic record, which includes possible biological activity. The SAM instrument analyzed drilled samples CH and MJ from the Pahrump Hills member and detected pyrolysis products, including thiophenic, aromatic, and aliphatic compounds released at temperatures of 500 °C to 820 °C. Some of these organic molecules contained sulfur in their structures, suggesting sulfurization from interaction with acid-sulfate fluids aided organic matter preservation [16]. Eigenbrode et al., [16] report that the diversity and composition of molecular contributions seen in MJ and CH samples are consistent with pyrolysis of geologically refractory organic macromolecules found in carbonaceous chondrites [152,153], kerogens [154], and coals [155,156]. Phyllosilicate abundance was low in the Pahrump Hills member, suggesting that they may not have played a role in organic preservation, however it is possible that phyllosilicates which were originally part of the sediment have been altered by diagenesis [98]. SAM recently performed a wet-chemistry experiment with the smectite-rich sample MA3 from GT [157]. Results from this experiment are currently being processed by the SAM team, but an abundance and/or diversity of organics in conjunction with high smectite content may signify the ability of smectite to preserve organics on Mars.

The alteration and transformation of rocks could compromise the integrity of organic preservation on Mars, and therefore those rocks that display low levels of diagenesis are considered priorities for potentially preserved organics [107]. Alteration post lithification has been observed in Gale crater, in some cases with rocks recording multiple alteration episodes, and Ca-sulfate filled fractures and veins are common in host rocks (e.g., [5,158–161]). Alteration halos have been identified along fractures in mudstone and sandstone in Gale crater and may represent multiple stages of aqueous alteration [105,162]. Understanding the alteration and overprinting from diagenetic events in Gale crater sediments is key to determining the habitability potential of phyllosilicate-bearing terrains on Mars.

6.4. Global Perspective and Implications for Sample Return and Future Planetary Missions

In situ measurements of phyllosilicates provide important ground-truthing of orbital observations and confirm detections and rough abundance estimates from orbital spectra [3,163] (Figure 4). Phyllosilicates have been detected in Jezero crater, and measurements made by *Curiosity* can be compared to those collected by *Perseverance* at Jezero crater to evaluate changes in phyllosilicate structure and composition over space and time. *Perseverance*, unfortunately, does not have a quantitative mineralogical instrument like CheMin. However, Raman and chemical measurements on *Perseverance* can be used to identify phyllosilicates, but it could be challenging to quantify mineral abundances with these datasets.

Phyllosilicate detections by CheMin can help inform the curation of future planned returned samples as part of the Mars Sample Return missions. Hydrated phases, like

smectite, can be sensitive to changes in temperature and relative humidity (e.g., [164]). The potential prevalence of collapsed smectites observed by CheMin suggests planned samples collected by Perseverance from smectite-bearing terrains in Jezero may also have collapsed smectite. These samples would have to be kept under desiccating conditions after collection and return to Earth to prevent hydration and cation exchange, which is critical to sample preservation. Similarly, samples that contain hydrated minerals (e.g., gypsum) will need to be kept under specific temperature and relative humidity conditions to prevent dehydration. This may be difficult to achieve within the sample tubes after collection and caching on the Martian surface. Diurnal and temperature fluctuations may cause the dehydration of some phases and the adsorption of H₂O by others, like smectite. An in-depth characterization of each sample target is essential before drilling and caching because the mineral assemblage may change slightly before the sample tubes are opened on Earth. These planned returned samples would benefit from a comprehensive characterization of in-depth mineralogy immediately upon return through the use of techniques like micro-XRD and transmission electron microscopy for structural characterization to evaluate the mineral assemblage and identify potential mineralogical changes since collection.

CheMin is the only XRD currently on any other planet, and data returned from CheMin have demonstrated the power of definitive quantitative mineralogy for interpreting the geologic history and habitability of a site on Mars. More advanced X-ray diffractometers are being developed for the future exploration of Mars, Venus, and other planetary bodies [165]. These instruments will have an improved angular resolution and angular range compared to MSL-CheMin and can be paired with XRF such that quantitative mineralogy and geochemistry can be measured from the same sample. These improvements can aid in the identification of phyllosilicates by possibly including the d(060) peak to better characterize phyllosilicate structure and to improve the accuracy of mass balance calculations from which phyllosilicate chemistry can be estimated. Developing a method to perform glycolation or heat treatments on clay-bearing samples within an X-ray diffractometer would further improve phyllosilicate identifications on other planets.

Author Contributions: The review paper summarizes the findings of numerous studies from the MSL team, instrument teams, and in the laboratory. All co-authors were involved with at least one of the following individual projects reviewed in this paper: conceptualization, methodology, formal analysis, investigation, data curation. Conceptualization, E.B.R., T.F.B., M.T.T., A.A.F., L.A.E., A.M., C.B., C.N.A., D.B., S.J.C., P.I.C., D.J.D.M., V.F., J.P.G., D.W.M., R.V.M., S.M.M., J.E., T.S.P., P.C.S., B.S., A.H.T., D.T.V., A.R.V., A.S.Y., J.C.B.; methodology, E.B.R., T.F.B., M.T.T., A.A.F., L.A.E., A.M., C.B., C.N.A., D.B., S.J.C., P.I.C., D.J.D.M., V.F., J.P.G., D.W.M., R.V.M., S.M.M., T.S.P., P.C.S., B.S., A.H.T., D.T.V., A.R.V., A.S.Y.; formal analysis, V.M.T., E.B.R., T.F.B., M.T.T., N.C., A.A.F., L.A.E., A.M., C.B., C.N.A., D.B., S.J.C., P.I.C., D.J.D.M., G.W.D., R.T.D., V.F., J.P.G., R.M.H., D.W.M., R.V.M., S.M.M., T.S.P., B.S., A.H.T., D.T.V., A.S.Y.; investigation, V.M.T., E.B.R., T.F.B., M.T.T., N.C., A.A.F., L.A.E., A.M., C.B., C.N.A., D.B., S.J.C., P.I.C., D.J.D.M., G.W.D., R.T.D., V.F., J.P.G., R.M.H., D.W.M., R.V.M., S.M.M., J.E., T.S.P., B.S., A.H.T., D.T.V., A.R.V., A.S.Y., J.C.B.; data curation, E.B.R., T.F.B., A.A.F., L.A.E., A.M., C.B., C.N.A., V.F., J.P.G., D.T.V., A.S.Y.; writing—original draft preparation, V.M.T., E.B.R., T.F.B., A.A.F., L.A.E., A.M., C.B., V.F.; writing—review and editing, V.M.T., E.B.R., T.F.B., M.T.T., J.V.C., A.A.F., L.A.E., A.M., C.B., V.F., R.M.H., B.P., J.E., D.T.V., A.R.V., J.C.B.; visualization, V.M.T., J.V.C., V.F., L.A.E. All authors have read and agreed to the published version of the manuscript.

Funding: The research reviewed in this paper was funded by the Mars Science Laboratory (MSL) project office. A.A.F. was supported by the NASA Mars Science Laboratory Participating Scientist Program. Additionally, a portion of this research was carried out at the Jet Propulsion Laboratory, California Institute of Technology, under a contract with the National Aeronautics and Space Administration (80NM0018D0004).

Data Availability Statement: Publicly available datasets were analyzed in this study. This data can be found here: [<https://pds.nasa.gov>], accessed on 23 July 2021. Additional contextual information can be found in the publically available CheMin Database found here: [<https://odr.io/chemin>], accessed on 23 July 2021.

Acknowledgments: The authors are grateful to the entire MSL team, instrument teams, engineers, and scientists that made the mission and studies possible.

Conflicts of Interest: The authors declare no conflict of interest. The funders had no role in the design of the study; in the collection, analyses, or interpretation of data; in the writing of the manuscript in the decision to publish the results.

Appendix A

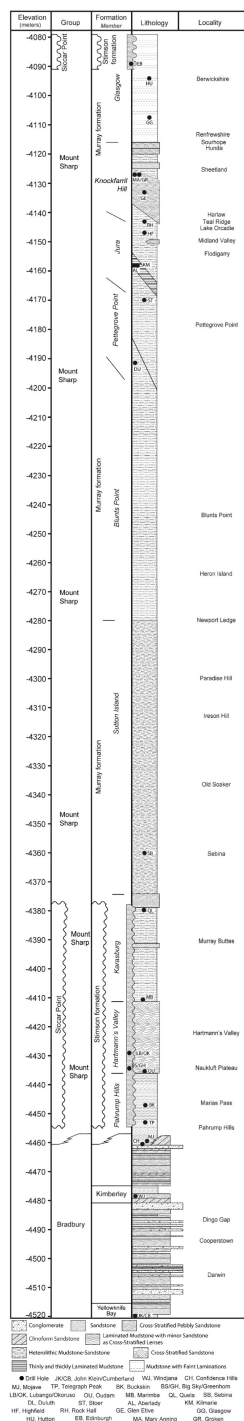


Figure A1. Detailed stratigraphic column of the sedimentary rocks at Gale crater from the MSL sedimentary and stratigraphy working group. The stratigraphic column reflects the units and formations investigated by *Curiosity* from the landing site near Yellowknife Bay through the Murray formation, Glasgow member.

References

1. Thomson, B.J.; Bridges, N.T.; Milliken, R.; Baldrige, A.; Hook, S.J.; Crowley, J.K.; Marion, G.K.; de Souza Filho, C.E.; Brown, A.J.; Weitz, C.M. Constraints on the origin and evolution of the layered mound in Gale Crater, Mars using Mars Reconnaissance Orbiter data. *Icarus* **2011**, *214*, 413–432. [[CrossRef](#)]
2. Grotzinger, J.P.; Crisp, J.; Vasavada, A.R.; Anderson, R.C.; Baker, C.J.; Barry, R.; Blake, D.F.; Conrad, P.; Edgett, K.S.; Ferdowski, B. Mars Science Laboratory mission and science investigation. *Space Sci. Rev.* **2012**, *170*, 5–56. [[CrossRef](#)]
3. Milliken, R.; Grotzinger, J.; Thomson, B. Paleoclimate of Mars as captured by the stratigraphic record in Gale Crater. *Geophys. Res. Lett.* **2010**, *37*. [[CrossRef](#)]
4. Grotzinger, J.P. Habitability, Taphonomy, and the Search for Organic Carbon on Mars: Introduction to Special Issue. *Science* **2014**, *343*, 386–389. [[CrossRef](#)]
5. Grotzinger, J.P.; Gupta, S.; Malin, M.C.; Rubin, D.M.; Schieber, J.; Siebach, K.; Sumner, D.Y.; Stack, K.M.; Vasavada, A.R.; Arvidson, R.E.; et al. Deposition, exhumation, and paleoclimate of an ancient lake deposit, Gale crater, Mars. *Science* **2015**, *350*, aac7575. [[CrossRef](#)] [[PubMed](#)]
6. Stack, K.M.; Grotzinger, J.P.; Lamb, M.P.; Gupta, S.; Rubin, D.M.; Kah, L.C.; Edgar, L.A.; Fey, D.M.; Hurowitz, J.A.; McBride, M. Evidence for plunging river plume deposits in the Pahrump Hills member of the Murray formation, Gale crater, Mars. *Sedimentology* **2019**, *66*, 1768–1802. [[CrossRef](#)]
7. Fedo, C.; Grotzinger, J.; Gupta, S.; Banham, S.; Bennett, K.; Edgar, L.; Fox, V.; Fraeman, A.; House, C.; Lewis, K. Evidence for persistent, water-rich, lacustrine deposition preserved in the Murray Formation, Gale crater: A depositional system suitable for sustained habitability. In Proceedings of the LPI Contributions, Ninth International Conference on Mars, Pasadena, CA, USA, 22–25 July 2019; Volume 2089, p. 6308.
8. Rivera-Hernández, F.; Sumner, D.Y.; Mangold, N.; Banham, S.G.; Edgett, K.S.; Fedo, C.M.; Gupta, S.; Gwizd, S.; Heydari, E.; Maurice, S. Grain size variations in the murray formation: Stratigraphic evidence for changing depositional environments in Gale crater, mars. *J. Geophys. Res. Planets* **2020**, *125*. [[CrossRef](#)]
9. Edgar, L.A.; Fedo, C.M.; Gupta, S.; Banham, S.; Fraeman, A.A.; Grotzinger, J.P.; Stack, K.; Stein, N.; Bennett, K.; Rivera-Hernández, F. A lacustrine paleoenvironment recorded at Vera Rubin Ridge, Gale crater: Overview of the sedimentology and stratigraphy observed by the Mars Science Laboratory Curiosity Rover. *J. Geophys. Res. Planets* **2020**, *125*. [[CrossRef](#)]
10. Vaniman, D.; Bish, D.; Ming, D.; Bristow, T.; Morris, R.; Blake, D.; Chipera, S.; Morrison, S.; Treiman, A.; Rampe, E. Mineralogy of a mudstone at Yellowknife Bay, Gale crater, Mars. *Science* **2014**, *343*. [[CrossRef](#)]
11. Bristow, T.F.; Rampe, E.B.; Achilles, C.N.; Blake, D.F.; Chipera, S.J.; Craig, P.; Crisp, J.A.; Des Marais, D.J.; Downs, R.T.; Gellert, R.; et al. Clay mineral diversity and abundance in sedimentary rocks of Gale crater, Mars. *Sci. Adv.* **2018**, *4*, eaar3330. [[CrossRef](#)] [[PubMed](#)]
12. Thorpe, M.; Bristow, T.; Rampe, E.; Grotzinger, J.; Fox, V.; Bennett, K.; Bryk, A.; Yen, A.; Vasavada, A.; Vaniman, D. The Mineralogy and Sedimentary History of the Glen Torridon Region, Gale Crater, Mars. In Proceedings of the 52nd Lunar and Planetary Science Conference, held virtually, 15–19 March 2021; p. 1519.
13. Ehlmann, B.L.; Mustard, J.F.; Fassett, C.I.; Schon, S.C.; Head, J.W., III; Des Marais, D.J.; Grant, J.A.; Murchie, S.L. Clay minerals in delta deposits and organic preservation potential on Mars. *Nat. Geosci.* **2008**, *1*, 355–358. [[CrossRef](#)]
14. Summons, R.E.; Amend, J.P.; Bish, D.; Buick, R.; Cody, G.D.; Des Marais, D.J.; Dromart, G.; Eigenbrode, J.L.; Knoll, A.H.; Sumner, D.Y. Preservation of martian organic and environmental records: Final report of the Mars Biosignature Working Group. *Astrobiology* **2011**, *11*, 157–181. [[CrossRef](#)]
15. Freissinet, C.; Glavin, D.; Mahaffy, P.R.; Miller, K.; Eigenbrode, J.; Summons, R.; Brunner, A.; Buch, A.; Szopa, C.; Archer, P., Jr. Organic molecules in the Sheepbed mudstone, Gale crater, Mars. *J. Geophys. Res. Planets* **2015**, *120*, 495–514. [[CrossRef](#)]
16. Eigenbrode, J.L.; Summons, R.E.; Steele, A.; Freissinet, C.; Millan, M.; Navarro-González, R.; Sutter, B.; McAdam, A.C.; Franz, H.B.; Glavin, D.P. Organic matter preserved in 3-billion-year-old mudstones at Gale crater, Mars. *Science* **2018**, *360*, 1096–1101. [[CrossRef](#)]
17. Gil-Lozano, C.; Fairén, A.G.; Muñoz-Iglesias, V.; Fernández-Sampedro, M.; Prieto-Ballesteros, O.; Gago-Duport, L.; Losa-Adams, E.; Carrizo, D.; Bishop, J.L.; Fornaro, T.; et al. Constraining the preservation of organic compounds in Mars analog nontronites after exposure to acid in alkaline fluids. *Sci. Rep.* **2020**, *10*, 1–11. [[CrossRef](#)] [[PubMed](#)]
18. Bishop, J.L.; Loizeau, D.; McKeown, N.K.; Saper, L.; Dyar, M.D.; De Marais, D.J.; Parente, M.; Murchie, S.L. What the ancient phyllosilicates at Mawrth Vallis can tell us about possible habitability on early Mars. *Planet. Space Sci.* **2013**, *86*, 130–149. [[CrossRef](#)]
19. Bibring, J.-P.; Langevin, Y.; Gendrin, A.; Gondet, B.; Poulet, F.; Berthé, M.; Soufflot, A.; Arvidson, R.; Mangold, N.; Mustard, J.; et al. Mars surface diversity as revealed by the OMEGA/Mars Express observations. *Science* **2005**, *307*, 1576–1581. [[CrossRef](#)]
20. Mustard, J.F.; Murchie, S.L.; Pelkey, S.; Ehlmann, B.; Milliken, R.; Grant, J.A.; Bibring, J.-P.; Poulet, F.; Bishop, J.; Dobrea, E.N. Hydrated silicate minerals on Mars observed by the Mars Reconnaissance Orbiter CRISM instrument. *Nature* **2008**, *454*, 305–309. [[CrossRef](#)]
21. Ehlmann, B.L.; Edwards, C.S. Mineralogy of the Martian surface. *Annu. Rev. Earth Planet. Sci.* **2014**, *42*. [[CrossRef](#)]
22. Wray, J.J.; Murchie, S.L.; Squyres, S.W.; Seelos, F.P.; Tornabene, L.L. Diverse aqueous environments on ancient Mars revealed in the southern highlands. *Geology* **2009**, *37*, 1043–1046. [[CrossRef](#)]

23. Bristow, T.F.; Bish, D.L.; Vaniman, D.T.; Morris, R.V.; Blake, D.F.; Grotzinger, J.P.; Rampe, E.B.; Crisp, J.A.; Achilles, C.N.; Ming, D.W.; et al. The origin and implications of clay minerals from Yellowknife Bay, Gale crater, Mars. *Am. Miner.* **2015**, *100*, 824–836. [[CrossRef](#)] [[PubMed](#)]
24. Poulet, F.; Bibring, J.-P.; Mustard, J.F.; Gendrin, A.; Mangold, N.; Langevin, Y.; Arvidson, R.E.; Gondet, B.; Gomez, C. Phyllosilicates on Mars and implications for early Martian climate. *Nature* **2005**, *438*, 623–627. [[CrossRef](#)] [[PubMed](#)]
25. Carter, J.; Poulet, F.; Bibring, J.P.; Murchie, S. Detection of hydrated silicates in crustal outcrops in the northern plains of Mars. *Science* **2010**, *328*, 1682–1686. [[CrossRef](#)]
26. Blake, D.; Vaniman, D.; Achilles, C.; Anderson, R.; Bish, D.; Bristow, T.; Chen, C.; Chipera, S.; Crisp, J.; Des Marais, D. Characterization and calibration of the CheMin mineralogical instrument on Mars Science Laboratory. *Space Sci. Rev.* **2012**, *170*, 341–399. [[CrossRef](#)]
27. Ming, D.W.; Gellert, R.; Morris, R.V.; Arvidson, R.E.; Brueckner, J.; Clark, B.C.; Cohen, B.A.; d’Uston, C.; Economou, T.; Fleischer, I.; et al. Geochemical properties of rocks and soils in Gusev crater, Mars: Results of the Alpha Particle X-ray Spectrometer from Cumberland Ridge to Home Plate. *JGR Planets* **2008**, *113*, E12. [[CrossRef](#)]
28. Guggenheim, S.; Martin, R.T. Definition of clay and clay mineral: Joint report of the AIPEA nomenclature and CMS nomenclature committees. *Clays Clay Miner.* **2005**, *43*, 255–256. [[CrossRef](#)]
29. Weaver, C.E. *Clays, Mud and Shales*; Elsevier: New York, NY, USA, 1989; p. 810.
30. Chamley, H. *Clay Mineralogy*; Springer: Berlin, Germany, 1989; p. 623.
31. Bristow, T.F.; Milliken, R.E. Terrestrial perspective on authigenic clay mineral production in ancient martian lakes. *Clays Clay Miner.* **2011**, *59*, 339–358. [[CrossRef](#)]
32. Faure, G. *Principles and Applications of Geochemistry*; Prentice Hall: Upper Saddle River, NJ, USA, 1997; p. 625.
33. Meunier, A. *Clays*; Springer: Berlin, Germany, 2005; p. 472.
34. Ehlmann, B.L.; Mustard, J.F.; Murchie, S.L.; Bibring, J.-P.; Meunier, A.; Fraeman, A.A.; Langevin, Y. Subsurface water and clay mineral formation during the early history of Mars. *Nature* **2011**, *479*, 53–60. [[CrossRef](#)]
35. Carter, J.; Poulet, F.; Bibring, J.P.; Mangold, N.; Murchie, S. Hydrous minerals on Mars as seen by the CRISM and OMEGA imaging spectrometers: Updated global view. *JGR Planets* **2013**, *118*, 831–858. [[CrossRef](#)]
36. Hicks, L.J.; Bridges, J.C.; Gurman, S.J. Ferric saponite and serpentine in the nakhlite martian meteorites. *GCA* **2014**, *136*, 194–210. [[CrossRef](#)]
37. Laird, D.A. Layer Charge Influences on the Hydration of Expandable 2:1 Phyllosilicates. *Clays Clay Miner.* **1999**, *47*, 630–636. [[CrossRef](#)]
38. Hedges, J.I.; Keil, R.G. Sedimentary organic matter preservation: An assessment and speculative synthesis. *Mar. Chem.* **1995**, *49*, 81–115. [[CrossRef](#)]
39. Mayer, L.M. Relationships between mineral surfaces and organic carbon concentrations in soils and sediments. *Chem. Geol.* **1994**, *114*, 347–363. [[CrossRef](#)]
40. Keil, R.G.; Mayer, L.M. Mineral matrices and organic matter. *Org. Geochem.* **2014**, *12*, 337.
41. Murchie, S.L.; Mustard, J.F.; Ehlmann, B.L.; Milliken, R.E.; Bishop, J.L.; McKeown, N.K.; Noe Dobrea, E.Z.; Seelos, F.P.; Buczkowski, D.L.; Wiseman, S.M.; et al. A synthesis of Martian aqueous mineralogy after 1 Mars year of observations from the Mars Reconnaissance Orbiter. *JGR Planets* **2009**, *114*, E2. [[CrossRef](#)]
42. Bishop, J.L.; Pieters, C.M.; Edwards, J.O. Infrared spectroscopic analyses on the nature of water in montmorillonite. *Clays Clay Miner.* **1994**, *42.6*, 702–716. [[CrossRef](#)]
43. Clark, R.N.; Swayze, G.A.; Singer, R.B.; Pollack, J.B. High-resolution reflectance spectra of Mars in the 2.3- μ m region: Evidence for the mineral scapolite. *JGR Solid Earth* **1990**, *95*, 14463–14480. [[CrossRef](#)]
44. Carter, J.; Poulet, F. Orbital identification of clays and carbonates in Gusev crater. *Icarus* **2012**, *219*, 250–253. [[CrossRef](#)]
45. Fox, V.; Arvidson, R.; Guinness, E.; McLennan, S.; Catalano, J.; Murchie, S.; Powell, K. Smectite deposits in Marathon Valley, Endeavour Crater, Mars, identified using CRISM hyperspectral reflectance data. *Geophys. Res. Lett.* **2016**, *43*, 4885–4892. [[CrossRef](#)]
46. Quantin-Nataf, C.; Carter, J.; Mandon, L.; Thollot, P.; Balme, M.; Volat, M.; Pan, L.; Loizeau, D.; Millot, C.; Breton, S. Oxia Planum: The Landing Site for the ExoMars “Rosalind Franklin” Rover Mission: Geological Context and Prelanding Interpretation. *Astrobiology* **2021**, *21*, 345–366. [[CrossRef](#)]
47. Williams, R.M.E.; Grotzinger, J.P.; Dietrich, W.E.; Gupta, S.; Sumner, D.Y.; Wiens, R.C.; Mangold, N.C.; Malin, M.C.; Edgett, K.S.; Maurice, S.; et al. Martian fluvial conglomerates at Gale crater. *Science* **2013**, *340*, 1068–1072. [[CrossRef](#)]
48. Edgar, L.A.; Gupta, S.; Rubin, D.M.; Lewis, K.W.; Kocurek, G.A.; Anderson, R.B.; Bell, J.F., III; Dromart, G.; Edgett, K.S.; Grotzinger, J.P.; et al. Shaler: In situ analysis of a fluvial sedimentary deposit on Mars. *Sedimentology* **2018**, *65*, 96–122. [[CrossRef](#)]
49. Fedo, C.; Grotzinger, J.; Gupta, S.; Fraeman, A.; Edgar, L.; Edgett, K.; Stein, N.; Rivera-Hernandez, F.; Lewis, K.; Stack, K. Sedimentology and stratigraphy of the Murray formation, Gale crater, Mars. In Proceedings of the 49th Lunar Planetary Science Conference, The Woodlands, TX, USA, 19–23 March 2018; p. 2083.
50. Rivera-Hernández, F.; Sumner, D.Y.; Mangold, N.; Stack, K.M.; Forni, O.; Newsom, H.; Williams, A.; Nachon, M.; l’Haridon, J.; Gasnault, O. Using ChemCam LIBS data to constrain grain size in rocks on Mars: Proof of concept and application to rocks at Yellowknife Bay and Pahrump Hills, Gale crater. *Icarus* **2019**, *321*, 82–98. [[CrossRef](#)]

51. Stein, N.; Grotzinger, J.; Schieber, J.; Mangold, N.; Hallet, B.; Newsom, H.; Stack, K.; Berger, J.; Thompson, J.; Siebach, K. Desiccation cracks provide evidence of lake drying on Mars, Sutton Island member, Murray formation, Gale Crater. *Geology* **2018**, *46*, 515–518. [[CrossRef](#)]
52. Gwizd, S.; Fedo, C.; Grotzinger, J.; Edgett, K.; Gupta, S.; Stack, K.; Banham, S.; Edgar, L.; Sumner, D. Toward a Greater Understanding of Cross-Stratified Facies in the Hartmann's Valley Member of the Murray Formation, Gale Crater, Mars. *LPI Contrib.* **2019**, *2089*, 6183.
53. Banham, S.G.; Gupta, S.; Rubin, D.M.; Watkins, J.A.; Sumner, D.Y.; Edgett, K.S.; Grotzinger, J.P.; Lewis, K.P.; Edgar, L.A.; Stack-Morgan, K.M. Ancient Martian aeolian processes and palaeomorphology reconstructed from the Stimson formation on the lower slope of Aeolis Mons, Gale crater, Mars. *Sedimentology* **2018**, *65*, 993–1042. [[CrossRef](#)]
54. Rice, M.S.; Gupta, S.; Treiman, A.H.; Stack, K.M.; Calef, F.; Edgar, L.A.; Grotzinger, J.; Lanza, N.; Le Deit, L.; Lasue, J.; et al. Geologic overview of the Mars Science Laboratory rover mission at the Kimberley, Gale crater, Mars. *JGR Planets* **2017**, *122*, 2–20. [[CrossRef](#)]
55. Kikuchi, S.; Shibuya, T. Thermodynamic Constrains on Smectite and Iron Oxide Formation at Gale Crater, Mars: Insights into Potential Free Energy from Aerobic Fe Oxidation in Lake Water-Groundwater Mixing Zone. *Minerals* **2021**, *4*, 341. [[CrossRef](#)]
56. Price, A.; Pearson, V.K.; Schwenzer, S.P.; Miot, J.; Olsson-Francis, K. Nitrate-dependent iron oxidation; a potential Mars metabolism. *Front. Microbiol.* **2018**, *9*, 513. [[CrossRef](#)]
57. Tung, H.C.; Bramall, N.E.; Price, P.B. Microbial origin of excess methane in glacial ice and implications for life on Mars. *Proc. Natl. Acad. Sci. USA* **2005**, *102*, 18292018296. [[CrossRef](#)] [[PubMed](#)]
58. Macey, M.C.; Fox-Powell, M.; Ramkissoon, N.K.; Stephens, B.P.; Barton, T.; Schwenzer, S.P.; Pearson, V.K.; Cousins, C.R.; Olsson-Francis, K. The identification of sulfide oxidation as a potential metabolism driving primary production on late Noachian Mars. *Sci. Rep.* **2020**, *10*, 1–13. [[CrossRef](#)] [[PubMed](#)]
59. King, G.M. Carbon monoxide as a metabolic energy source for extremely halophilic microbes: Implications for microbial activity in Mars regolith. *Proc. Natl. Acad. Sci. USA* **2015**, *112*, 4465–4470. [[CrossRef](#)] [[PubMed](#)]
60. Edward, K.J.; Bach, W.; McCollum, T.M.; Rogers, D.R. Neutrophilic iron-oxidizing bacteria in the ocean: Their habitats, diversity, and roles in mineral deposition, rock alteration, and biomass production in the deep-sea. *Geomicrobiol. J.* **2004**, *21*, 393–404. [[CrossRef](#)]
61. Emerson, D.; Fleming, E.J.; McBeth, J.M. Iron-oxidizing bacteria: An environmental and genomic perspective. *Annu. Rev. Microbiol.* **2010**, *64*, 561–583. [[CrossRef](#)] [[PubMed](#)]
62. Popa, P.; Smith, A.R.; Popa, R.; Jane Boone, J.; Fisk, M. Olivine-respiring bacteria isolated from the rock-ice interface in a lava-tube cave, a Mars analog environment. *Astrobiology* **2012**, *12*, 9–18. [[CrossRef](#)]
63. Tosca, N.J.; Ahmed, I.A.; Tutolo, B.M.; Ashpittel, A.; Hurowitz, J.A. Magnetite authigenesis and the warming of early Mars. *Nat. Geosci.* **2018**, *11*, 635–639. [[CrossRef](#)]
64. Canfield, D.E.; Kristensen, E.; Thamdrup, B. *Aquatic Geomicrobiology*; Elsevier: Amsterdam, The Netherlands, 2005.
65. Ragsdale, S.W.; Pierce, E. Acetogenesis and the Wood-Ljungdahl pathway of CO₂ fixation. *Biochim. Biophys. Acta Proteins Proteom.* **2008**, *1784*, 1873–1898. [[CrossRef](#)] [[PubMed](#)]
66. Braakman, R.; Smith, E. The emergence and early evolution of biological carbon-fixation. *PLoS Comput. Biol.* **2012**, *8*, e1002455. [[CrossRef](#)]
67. Rampe, E.B.; Blake, D.F.; Bristow, T.F.; Ming, D.W.; Vaniman, D.T.; Morris, R.V.; Achilles, C.N.; Chipera, S.J.; Morrison, S.M.; Tu, V.M.; et al. Mineralogy and geochemistry of sedimentary rocks and eolian sediments in Gale crater, Mars: A review after six Earth years of exploration with *Curiosity*. *Geochemistry* **2020**, *80*, 125605. [[CrossRef](#)]
68. Fraeman, A.A.; Edgar, L.A.; Rampe, E.B.; Thompson, L.M.; Frydenvang, J.; Fedo, C.M.; Catalano, J.G.; Dietrich, W.E.; Gabriel, T.S.; Vasavada, A.R.; et al. Evidence for a diagenetic origin of Vera Rubin ridge, Gale crater, Mars: Summary and synthesis of *Curiosity's* exploration campaign. *J. Geophys. Res. Planets* **2020**, *125*, e2020JE006527. [[CrossRef](#)] [[PubMed](#)]
69. Dera, P.; Zhuravlev, K.; Prakapenka, V.; Rivers, M.L.; Finkelstein, G.J.; Grubor-Urosevic, O.; Tschauer, O.; Clark, M.; Downs, R.T. High pressure single-crystal micro X-ray diffraction analysis with GSE_ADA/RSV software. *High Press. Res.* **2013**, *33*, 466–484. [[CrossRef](#)]
70. Rietveld, H.M. A profile refinement method for nuclear and magnetic structures. *J. Appl. Crystallogr.* **1969**, *2*, 65–71. [[CrossRef](#)]
71. Bish, D.L.; Howard, S. Quantitative phase analysis using the Rietveld method. *J. Appl. Crystallogr.* **1988**, *21*, 86–91. [[CrossRef](#)]
72. Bish, D.L.; Post, J.E. (Eds.) *Modern Powder Diffraction*; De Gruyter: Berlin, Germany, 1989.
73. Morrison, S.M.; Downs, R.T.; Blake, D.F.; Vaniman, D.T.; Ming, D.W.; Hazen, R.M.; Treiman, A.H.; Achilles, C.N.; Yen, A.S.; Morris, R.V.; et al. Crystal chemistry of martian minerals from Bradbury Landing through Nauklufft Plateau, Gale crater, Mars. *Am. Min. J. Earth Planet. Mater.* **2018**, *103*, 857–871. [[CrossRef](#)]
74. Moore, D.M.; Reynolds, R.C., Jr. *X-ray Diffraction and the Identification and Analysis of Clay Minerals*, 2nd ed.; Oxford University Press: Oxford, UK; New York, NY, USA, 1997; p. 382.
75. Morris, R.V.; Ming, D.; Blake, D.; Vaniman, D.; Bish, D.; Chipera, S.; Downs, R.; Gellert, R.; Treiman, A.; Yen, A. The Amorphous Component in Martian Basaltic Soil in Global Perspective from MSL and MER Missions. In Proceedings of the 44th Lunar and Planetary Science Conference, The Woodlands, TX, USA, 18–22 March 2013.
76. Chipera, S.J.; Bish, D.L. FULLPAT: A full-pattern quantitative analysis program for X-ray powder diffraction using measured and calculated patterns. *J. Appl. Crystallogr.* **2002**, *35*, 744–749. [[CrossRef](#)]

77. Chipera, S.J.; Bish, D.L. Fitting full X-ray diffraction patterns for quantitative analysis: A method for readily quantifying crystalline and disordered phases. *AMPC* **2013**, *3*, 47–53. [[CrossRef](#)]
78. Leshin, L.; Mahaffy, P.; Webster, C.; Cabane, M.; Coll, P.; Conrad, P.; Archer, P.; Atreya, S.; Brunner, A.; Buch, A. Volatile, isotope, and organic analysis of martian fines with the Mars *Curiosity* rover. *Science* **2013**, *341*. [[CrossRef](#)] [[PubMed](#)]
79. Glavin, D.P.; Freissinet, C.; Miller, K.E.; Eigenbrode, J.L.; Brunner, A.E.; Buch, A.; Sutter, B.; Archer, P.D., Jr.; Atreya, S.K.; Brinckerhoff, W.B. Evidence for perchlorates and the origin of chlorinated hydrocarbons detected by SAM at the Rocknest aeolian deposit in Gale Crater. *J. Geophys. Res. Planets* **2013**, *118*, 1955–1973. [[CrossRef](#)]
80. Sutter, B.; Mcadam, A.C.; Mahaffy, P.R.; Ming, D.W.; Edgett, K.E.; Rampe, E.B.; Eigenbrode, J.L.; Franz, H.B.; Freissinet, C.; Grotzinger, J.P. Evolved gas analyses of sedimentary rocks and eolian sediment in Gale Crater, Mars: Results of the *Curiosity* rover's sample analysis at Mars instrument from Yellowknife Bay to the Namib Dune. *J. Geophys. Res. Planets* **2017**, *122*, 2574–2609. [[CrossRef](#)]
81. Bish, D.; Duffy, C. Thermogravimetric analysis of minerals. *Therm. Anal. Clay Sci.* **1990**, *3*, 96–157.
82. Maurice, S.; Wiens, R.; Saccoccio, M.; Barraclough, B.; Gasnault, O.; Forni, O.; Mangold, N.; Baratoux, D.; Bender, S.; Berger, G. The ChemCam instrument suite on the Mars Science Laboratory (MSL) rover: Science objectives and mast unit description. *Space Sci. Rev.* **2012**, *170*, 95–166. [[CrossRef](#)]
83. Wiens, R.C.; Maurice, S.; Barraclough, B.; Saccoccio, M.; Barkley, W.C.; Bell, J.F.; Bender, S.; Bernardin, J.; Blaney, D.; Blank, J. The ChemCam instrument suite on the Mars Science Laboratory (MSL) rover: Body unit and combined system tests. *Space Sci. Rev.* **2012**, *170*, 167–227. [[CrossRef](#)]
84. Clegg, S.M.; Wiens, R.C.; Anderson, R.; Forni, O.; Frydenvang, J.; Lasue, J.; Cousin, A.; Payre, V.; Boucher, T.; Dyar, M.D. Recalibration of the Mars Science Laboratory ChemCam instrument with an expanded geochemical database. *Spectrochim. Acta Part. B At. Spectrosc.* **2017**, *129*, 64–85. [[CrossRef](#)]
85. Meslin, P.-Y.; Gasnault, O.; Forni, O.; Schröder, S.; Cousin, A.; Berger, G.; Clegg, S.; Lasue, J.; Maurice, S.; Sautter, V. Soil diversity and hydration as observed by ChemCam at Gale Crater, Mars. *Science* **2013**, *341*. [[CrossRef](#)] [[PubMed](#)]
86. Le Mouélic, S.; Gasnault, O.; Herkenhoff, K.; Bridges, N.; Langevin, Y.; Mangold, N.; Maurice, S.; Wiens, R.; Pinet, P.; Newsom, H. The ChemCam Remote Micro-Imager at Gale crater: Review of the first year of operations on Mars. *Icarus* **2015**, *249*, 93–107. [[CrossRef](#)]
87. Frydenvang, J.; Mangold, N.; Wiens, R.C.; Fraeman, A.A.; Edgar, L.A.; Fedo, C.M.; L'Haridon, J.; Bedford, C.C.; Gupta, S.; Grotzinger, J.P. The chemostratigraphy of the Murray formation and role of diagenesis at Vera Rubin ridge in Gale crater, Mars, as observed by the ChemCam instrument. *J. Geophys. Res. Planets* **2020**, *125*, e2019JE006320. [[CrossRef](#)]
88. Bedford, C.; Bridges, J.; Schwenzer, S.; Wiens, R.C.; Rampe, E.; Frydenvang, J.; Gasda, P.J. Alteration trends and geochemical source region characteristics preserved in the fluvio-lacustrine sedimentary record of Gale crater, Mars. *GCA* **2019**, *246*, 234–266. [[CrossRef](#)]
89. Mangold, N.; Dehouck, E.; Fedo, C.; Forni, O.; Achilles, C.; Bristow, T.; Downs, R.; Frydenvang, J.; Gasnault, O.; L'haridon, J. Chemical alteration of fine-grained sedimentary rocks at Gale crater. *Icarus* **2019**, *321*, 619–631. [[CrossRef](#)]
90. Le Deit, L.; Mangold, N.; Forni, O.; Cousin, A.; Lasue, J.; Schröder, S.; Wiens, R.C.; Sumner, D.; Fabre, C.; Stack, K.M. The potassic sedimentary rocks in Gale Crater, Mars, as seen by ChemCam on board *Curiosity*. *J. Geophys. Res. Planets* **2016**, *121*, 784–804. [[CrossRef](#)]
91. Mangold, N.; Forni, O.; Dromart, G.; Stack, K.; Wiens, R.C.; Gasnault, O.; Sumner, D.Y.; Nachon, M.; Meslin, P.Y.; Anderson, R.B. Chemical variations in Yellowknife Bay formation sedimentary rocks analyzed by ChemCam on board the *Curiosity* rover on Mars. *J. Geophys. Res. Planets* **2015**, *120*, 452–482. [[CrossRef](#)]
92. Anderson, S.; Ehlmann, B.; Morris, R.; McLennan, S.; Boucher, T.; Dyar, M.; McInroy, R.; Delapp, D.; Wiens, R.; Frydenvang, J. Expanded Compositional Database for ChemCam Quantitative Calibration. RB. In Proceedings of the 8th International Conference on Mars, Pasadena, CA, USA, 14–18 July 2014.
93. Mangold, J.E.; Park, C.M.; Liljeström, H.M.; Katz, L.E. Surface complexation modeling of Hg (II) adsorption at the goethite/water interface using the Charge Distribution Multi-Site Complexation (CD-MUSIC) model. *J. Colloid Interface Sci.* **2014**, *418*, 147–161. [[CrossRef](#)] [[PubMed](#)]
94. McLennan, S.M.; Anderson, R.; Bell, J.; Bridges, J.C.; Calef, F.; Campbell, J.L.; Clark, B.; Clegg, S.; Conrad, P.; Cousin, A. Elemental geochemistry of sedimentary rocks at Yellowknife Bay, Gale crater, Mars. *Science* **2014**, *343*. [[CrossRef](#)] [[PubMed](#)]
95. Ollila, A.M.; Newsom, H.E.; Clark, B., III.; Wiens, R.C.; Cousin, A.; Blank, J.G.; Mangold, N.; Sautter, V.; Maurice, S.; Clegg, S.M. Trace element geochemistry (Li, Ba, Sr, and Rb) using *Curiosity's* ChemCam: Early results for Gale crater from Bradbury landing site to Rocknest. *J. Geophys. Res. Planets* **2014**, *119*, 255–285. [[CrossRef](#)]
96. Gellert, R.; Yen, A.S. Elemental Analyses of Mars from Rovers Using the Alpha-Particle X-Ray Spectrometer. *Remote Compos. Anal. Tech. Underst. Spectrosc.* **2019**, 555–572. [[CrossRef](#)]
97. Gellert, R.; Campbell, J.L.; King, P.L.; Leshin, L.A.; Lugmair, G.W.; Spray, J.G.; Squyres, S.W.; Yen, A.S. The alpha-particle-x-ray-spectrometer (apxs) for the mars science laboratory (msl) rover mission. In Proceedings of the 40th Lunar and Planetary Science Conference, LPI Contribution, Woodlands, TX, USA, 23–27 March 2009; Volume 1468, p. 2364.
98. Achilles, C.N.; Rampe, E.B.; Downs, R.T.; Bristow, T.F.; Ming, D.W.; Morris, R.V.; Vaniman, D.T.; Blake, D.F.; McAdam, A.C.; Sutter, B. Evidence for multiple diagenetic episodes in ancient fluvial-lacustrine sedimentary rocks in Gale crater, Mars. *JGR Planets* **2020**, *125*, e2019JE006295. [[CrossRef](#)]

99. Vaniman, D.T.; Martinex, G.M.; Rampe, E.B.; Bristow, T.F.; Blake, D.F.; Yen, A.S.; Ming, D.W.; Rapin, W.; Meslin, P.Y.; Morookian, J.M.; et al. Gypsum, basanite, and anhydrite at Gale crater, Mars. *Am. Min. J. Earth Planet. Mater.* **2018**, *103*, 1011–1020.
100. Blake, D.F.; Morris, R.V.; Kocurek, G.; Morrison, S.M.; Downs, R.T.; Bish, D.; Ming, D.W.; Edgett, K.S.; Rubin, D.; Goetz, W.; et al. *Curiosity* at Gale crater, Mars: Characterization and analysis of the Rocknest sand shadow. *Science* **2013**, *341*, 6153. [[CrossRef](#)]
101. Treiman, A.H.; Bish, D.L.; Vaniman, D.T.; Chipera, S.J.; Blake, D.F.; Ming, D.W.; Morris, R.V.; Bristow, T.F.; Morrison, S.M.; Baker, M.B. Mineralogy, provenance, and diagenesis of a potassic basaltic sandstone on Mars: CheMin X-ray diffraction of the Windjana sample (Kimberley area, Gale Crater). *J. Geophys. Res. Planets* **2016**, *121*, 75–106. [[CrossRef](#)] [[PubMed](#)]
102. Rampe, E.; Ming, D.; Blake, D.; Bristow, T.; Chipera, S.; Grotzinger, J.; Morris, R.; Morrison, S.; Vaniman, D.; Yen, A. Mineralogy of an ancient lacustrine mudstone succession from the Murray formation, Gale crater, Mars. *EPSL* **2017**, *471*, 172–185. [[CrossRef](#)]
103. Morris, R.V.; Vaniman, D.T.; Blake, D.F.; Gellert, R.; Chipera, S.J.; Rampe, E.B.; Ming, D.W.; Morrison, S.M.; Downs, R.T.; Treiman, A.H.; et al. Silicic volcanism on Mars evidenced by tridymite in high-SiO₂ sedimentary rock at Gale crater. *Proc. Natl. Acad. Sci. USA* **2016**, *113*, 7071–7076. [[CrossRef](#)] [[PubMed](#)]
104. Morris, R.V.; Bristow, T.F.; Rampe, E.B.; Yen, A.S.; Vaniman, D.T.; Tu, V.; Thorpe, M.T.; Peretyazhko, T.S.; Morrison, S.M.; Ming, D.W.; et al. Mineralogy and formation processes for the Vera Rubin Ridge at Gale crater, Mars from CheMin and XRD analyses. In Proceedings of the Lunar and Planetary Science Conference, Houston, TX, USA, 18–22 March 2019.
105. Yen, A.S.; Ming, D.W.; Vaniman, D.T.; Gellert, R.; Blake, D.F.; Morris, R.V.; Morrison, S.M.; Bristow, T.F.; Chipera, S.J.; Edgett, K.S.; et al. Multiple stages of aqueous alteration along fractures in mudstone and sandstone strata in Gale Crater, Mars. *EPSL* **2017**, *471*, 186–198. [[CrossRef](#)]
106. Rampe, E.B.; Lapotre, M.G.A.; Bristow, T.F.; Arvidson, R.E.; Morris, R.V.; Achilles, C.N.; Weitz, C.; Blake, D.F.; Ming, D.W.; Morrison, S.M.; et al. Sand mineralogy within the Bagnold Dunes, Gale crater, as observed in situ and from orbit. *Geophys. Res. Lett.* **2018**, *45*, 9488–9497. [[CrossRef](#)]
107. Bristow, T.F.; Grotzinger, J.P.; Rampe, E.B.; Cuadros, J.; Chipera, S.J.; Downs, G.; Fedo, C.M.; Frydenvang, J.; McAdam, A.C.; Morris, R.V.; et al. Brine Driven Destruction of Clay Minerals in Gale Crater Mars. *Science* **2021**. [[CrossRef](#)]
108. L veill , R.J.; Bridges, J.; Wiens, R.C.; Mangold, N.; Cousin, A.; Lanza, N.; Forni, O.; Ollila, A.; Grotzinger, J.; Clegg, S.; et al. Chemistry of fracture-filling raised ridges in Yellowknife Bay, Gale Crater: Window into past aqueous activity and habitability on Mars. *J. Geophys. Res. Planets* **2014**, *119*, 2398–2415. [[CrossRef](#)]
109. Siebach, K.; Grotzinger, J.; Kah, L.; Stack, K.; Malin, M.; L veill , R.; Sumner, D. Subaqueous shrinkage cracks in the Sheepbed mudstone: Implications for early fluid diagenesis, Gale crater, Mars. *J. Geophys. Res. Planets* **2014**, *119*, 1597–1613. [[CrossRef](#)]
110. Stack, K.; Grotzinger, J.; Kah, L.; Schmidt, M.; Mangold, N.; Edgett, K.; Sumner, D.; Siebach, K.; Nachon, M.; Lee, R. Diagenetic origin of nodules in the Sheepbed member, Yellowknife Bay formation, Gale crater, Mars. *J. Geophys. Res. Planets* **2014**, *119*, 1637–1664. [[CrossRef](#)]
111. Treiman, A.H.; Morris, R.V.; Agresti, D.G.; Graff, T.G.; Achilles, C.N.; Rampe, E.B.; Bristow, T.F.; Ming, D.W.; Blake, D.F.; Vaniman, D.T.; et al. Ferrian saponite from the Santa Monica Mountains (California, USA, Earth): Characterization as an analog for clay minerals on Mars with application to Yellowknife Bay in Gale Crater. *Am. Min.* **2014**, *99*, 2234–2250. [[CrossRef](#)]
112. Ming, D.W.; Archer, P.; Glavin, D.; Eigenbrode, J.; Franz, H.; Sutter, B.; Brunner, A.; Stern, J.; Freissinet, C.; McAdam, A. Volatile and organic compositions of sedimentary rocks in Yellowknife Bay, Gale Crater, Mars. *Science* **2014**, *343*. [[CrossRef](#)]
113. Fedo, C.; Grotzinger, J.; Gupta, S.; Stein, N.; Watkins, J.; Banham, S.; Edgett, K.; Minitti, M.; Schieber, J.; Siebach, K. Facies analysis and basin architecture of the upper part of the Murray formation, Gale Crater, Mars. In Proceedings of the 48th Lunar and Planetary Science Conference, Houston, TX, USA, 20–24 March 2017; p. 1689.
114. Gwizd, S.; Fedo, C.; Grotzinger, J.; Edgett, K.; Rivera-Hernandez, F.; Stein, N. Depositional history of the Hartmann’s valley member, Murray formation, Gale crater, Mars. In Proceedings of the Lunar and Planetary Science Conference, Houston, TX, USA, 19–23 March 2018; p. 2150.
115. Stein, N.; Ehlmann, B.; Ammannito, E.; Palomba, E.; Desanctis, M.; Jaumann, R.; Nathues, A.; Raymond, C.; Hiesinger, H.; Schenk, P. Characteristics, formation, and evolution of Faculae (bright spots) on Ceres. In Proceedings of the 48th Lunar and Planetary Science Conference, Houston, TX, USA, 20–24 March 2017.
116. Craig, P.; Ming, D.; Rampe, E. Sulfate Formation From Acid-Weathered Phyllosilicates: Implications for the Aqueous History of Mars. In Proceedings of the Lunar and Planetary Science Conference, Houston, TX, USA, 17–21 March 2014.
117. Fraeman, A.; Ehlmann, B.; Arvidson, R.; Edwards, C.; Grotzinger, J.; Milliken, R.; Quinn, D.; Rice, M. The stratigraphy and evolution of lower Mount Sharp from spectral, morphological, and thermophysical orbital data sets. *J. Geophys. Res. Planets* **2016**, *121*, 1713–1736. [[CrossRef](#)]
118. Carter, J.; Gondet, B.; Langevin, Y. MSL Homing in on a large smectite clay deposit: An orbital perspective. In Proceedings of the Lunar and Planetary Science Conference, Houston, TX, USA, 21–25 March 2016; p. 1899.
119. Heller-Kallai, L.; Rozenson, L. Dehydroxylation of dioctahedral phyllosilicates. *Clays Clay Miner.* **1980**, *28*, 355–368. [[CrossRef](#)]
120. Derkowski, A.; Bristow, T.F. On the problems of total specific surface area and cation exchange capacity measurements in organic-rich sedimentary rocks. *Clays Clay Miner.* **2012**, *60*, 348–362. [[CrossRef](#)]
121. Cuadros, J.; Afsin, B.; Jadubansa, P.; Ardakani, M.; Ascaso, C.; Wierzbos, J.; Adams, J. Pathways of volcanic glass alteration in laboratory experiments through inorganic and microbially-mediated processes. *Clay Miner.* **2013**, *48*, 423–445. [[CrossRef](#)]

122. Rampe, E.B.; Bristow, T.F.; Morris, R.V.; Morrison, S.M.; Achilles, C.N.; Ming, D.W.; Vaniman, D.T.; Blake, D.F.; Tu, V.M.; Chipera, S.J.; et al. Mineralogy of Vera Rubin Ridge From the Mars Science Laboratory CheMin Instrument. *J. Geophys. Res. Planets* **2020**, *125*, e2019JE006306. [[CrossRef](#)]
123. Fraeman, A.; Arvidson, R.; Catalano, J.; Grotzinger, J.; Morris, R.; Murchie, S.; Stack, K.; Humm, D.; McGovern, J.; Seelos, F. A hematite-bearing layer in Gale Crater, Mars: Mapping and implications for past aqueous conditions. *Geology* **2013**, *41*, 1103–1106. [[CrossRef](#)]
124. Jacob, S.R.; Wellington, D.F.; Bell, J.F., III; Achilles, C.; Fraeman, A.A.; Horgan, B.; Johnson, J.R.; Maurice, S.; Peters, G.; Rampe, E.B.; et al. Spectral, compositional, and physical properties of the upper Murray formation and Vera Rubin ridge, Gale Crater, Mars. *J. Geophys. Res. Planets* **2020**, *125*, e2019JE006290. [[CrossRef](#)]
125. Berger, J.A.; Gellert, R.; Boyd, N.I.; King, P.L.; McCraig, M.A.; O’Connell-Cooper, C.D.; Schmidt, M.E.; Spray, J.G.; Thompson, L.M.; VanBommel, S.J.; et al. Elemental composition and chemical evolution of geologic materials in Gale Crater, Mars: APXS results from Bradbury landing to the Vera Rubin ridge. *J. Geophys. Res. Planets* **2020**, *125*, 12. [[CrossRef](#)]
126. McAdam, A.C.; Sutter, B.; Archer, P.D.; Franz, H.B.; Wong, G.M.; Lewis, J.M.; Eigenbrode, J.L.; Stern, J.C.; Knudson, C.A.; Clark, J.V. Constraints on the Mineralogy and Geochemistry of Vera Rubin Ridge, Gale Crater, Mars, From Mars Science Laboratory Sample Analysis at Mars Evolved Gas Analyses. *J. Geophys. Res. Planets* **2020**, *125*, e2019JE006309. [[CrossRef](#)]
127. Horgan, B.H.; Anderson, R.B.; Dromart, G.; Amador, E.S.; Rice, M.S. The mineral diversity of Jezero crater: Evidence for possible lacustrine carbonates on Mars. *Icarus* **2020**, *339*, 113526. [[CrossRef](#)]
128. Sheppard, R.Y.; Milliken, R.E.; Parente, M.E.; Itoh, Y. Updated perspectives and hypotheses on the mineralogy of lower Mt. Sharp, Mars, as seen from orbit. *J. Geophys. Res.* **2020**, *126*, e2020JE006372.
129. Fox, V.; Jacob, S.; Maurice, S.; Rampe, E.; Rice, M.; Seeger, C.; Wiens, R. Diagenesis in the Glen Torridon Region of Gale Crater, Mars Using VNIR Spectral Data From the *Curiosity* Rover. In Proceedings of the Lunar and Planetary Science Conference, LPI Contribution, Houston, TX, USA, 15–19 March 2021; Volume 2548, p. 1502.
130. Bedford, C.C.; Schwenger, S.P.; Bridges, J.C.; Banham, S.; Wiens, R.C.; Gasnault, O.; Rampe, E.B.; Frydenvang, J.; Gasda, P.J. Geochemical variation in the Stimson formation of Gale crater: Provenance, mineral sorting, and a comparison with modern Martian dunes. *Icarus* **2020**, *341*, 113622. [[CrossRef](#)]
131. Banham, S.; Gupta, S.; Bryk, A.; Rubin, D.M.; Edgett, K.S.; Dietrich, W.; Caravaca, G.; Edgar, L.A.; Vasavada, A. Reconstructing Martian environmental change across a major unconformity at Gale crater: Sedimentology of the Stimson formation at the Greenheugh pediment. In Proceedings of the AGU Fall Meeting, Online, 1–17 December 2020.
132. Banham, S.; Sanjeev, G.; Rubin, D.M.; Edgett, K.S.; Barnes, R.; Van Beek, J.; Watkins, J.A.; Edgar, L.A.; Fedo, C.M.; Williams, R.M.; et al. A Rock Record of Complex Aeolian Bedforms in a Hesperian Desert Landscape: The Stimson Formation as Exposed in the Murray Buttes, Gale Crater, Mars. *J. Geophys. Res. Planets* **2021**, *126*, e2020JE006554. [[CrossRef](#)]
133. Gasda, P.J.; Haldeman, E.B.; Wiens, R.C.; Rapin, W.; Bristow, T.F.; Bridges, J.C.; Schwenger, S.P.; Clark, B.; Herkenhoff, K.; Frydenvang, J. In situ detection of boron by ChemCam on Mars. *Geophys. Res. Lett.* **2017**, *44*, 8739–8748. [[CrossRef](#)]
134. Hurowitz, J.A.; Grotzinger, J.P.; Fischer, W.W.; McLennan, S.M.; Milliken, R.E.; Stein, N.; Vasavada, A.R.; Blake, D.; Dehouck, E.; Eigenbrode, J.L. Redox stratification of an ancient lake in Gale crater, Mars. *Science* **2017**, *356*. [[CrossRef](#)]
135. Che, C.; Glotch, T.D.; Bish, D.L.; Michalski, J.R.; Xu, W. Spectroscopic study of the dehydration and/or dehydroxylation of phyllosilicate and zeolite minerals. *JGR Planets* **2011**, *116*. [[CrossRef](#)]
136. Bibring, J.-P.; Langevin, Y.; Mustard, J.F.; Poulet, F.; Arvidson, R.; Gendrin, A.; Gondet, B.; Mangold, N.; Pinet, P.; Forget, F.; et al. Global mineralogical and aqueous Mars history derived from OMEGA/Mars Express data. *Science* **2006**, *312*, 400–404. [[CrossRef](#)]
137. Vicente, M.A.; Razzaghe, M.; Robert, M. Formation of aluminium hydroxy vermiculite (intergrade) and smectite from mica under acidic conditions. *Clay Miner.* **1977**, *12*, 101–112. [[CrossRef](#)]
138. Sutter, B.; Archer, P.D.; Ming, D.W.; Niles, P.B.; Eigenbrode, J.L.; Franz, H.; Glavin, D.P.; McAdam, A.C. The investigation of chlorates as a possible source of oxygen and chlorine detected by the sample analysis at Mars (SAM) instrument in Gale Crater, Mars. In Proceedings of the Lunar and Planetary Science Conference, Houston, TX, USA, 17–21 March 2014.
139. Peretyazhko, T.; Sutter, B.; Morris, R.; Agresti, D.; Le, L.; Ming, D. Fe/Mg smectite formation under acidic conditions on early Mars. *GCA* **2016**, *173*, 37–49. [[CrossRef](#)]
140. Peretyazhko, T.; Niles, P.; Sutter, B.; Morris, R.; Agresti, D.; Le, L.; Ming, D. Smectite formation in the presence of sulfuric acid: Implications for acidic smectite formation on early Mars. *GCA* **2018**, *220*, 248–260. [[CrossRef](#)] [[PubMed](#)]
141. Gainey, S.T.; Hausrath, E.M.; Adcock, C.T.; Tschauner, O.; Hurowitz, J.A.; Ehlmann, B.L.; Xiao, Y.; Bartlett, C.L. Clay mineral formation under oxidized conditions and implications for paleoenvironments and organic preservation on Mars. *Nat. Commun.* **2017**, *1*, 1–7. [[CrossRef](#)] [[PubMed](#)]
142. Bridges, J.C.; Schwenger, S.P. The Nakhilite Hydrothermal Brine. *EPSL* **2012**, *359*, 117–123. [[CrossRef](#)]
143. Harder, H. The role of magnesium in the formation of smectite minerals. *Chem. Geol.* **1972**, *10*, 31–39. [[CrossRef](#)]
144. Harder, H. Nontronite synthesis at low temperatures. *Chem. Geol.* **1976**, *18*, 169–180. [[CrossRef](#)]
145. Decarreau, A.; Bonnin, D. Synthesis and crystallogenesi s at low temperature of Fe (III)-smectites by evolution of coprecipitated gels: Experiments in partially reducing conditions. *Clay Miner.* **1986**, *21*, 861–877. [[CrossRef](#)]
146. Decarreau, A.; Bonnin, D.; Badaut-Trauth, D.; Couty, R.; Kaiser, P. Synthesis and crystallogenesi s of ferric smectite by evolution of Si-Fe coprecipitates in oxidizing conditions. *Clay Miner.* **1987**, *22*, 207–223. [[CrossRef](#)]

147. Vogels, R.; Kerkhoffs, M.; Geus, J. Non-hydrothermal synthesis, characterisation and catalytic properties of saponite clays. In *Studies in Surface Science and Catalysis*; Elsevier: Amsterdam, The Netherlands, 1995; pp. 1153–1161.
148. Fukushi, K.; Sekine, Y.; Sakuma, H.; Morida, K.; Wordsworth, R. Semiarid climate and hyposaline lake on early Mars inferred from reconstructed water chemistry at Gale. *Nat. Commun.* **2019**, *10*, 1–11. [[CrossRef](#)] [[PubMed](#)]
149. Schieber, J.; Bish, D.; Coleman, M.; Reed, M.; Hausrath, E.M.; Cosgrove, J.; Gupta, S.; Minitti, M.E.; Edgett, K.S.; Malin, M. Encounters with an unearthy mudstone: Understanding the first mudstone found on Mars. *Sedimentology* **2017**, *64*, 311–358. [[CrossRef](#)]
150. Michalopoulos, P.; Aller, R.C. Early diagenesis of biogenic silica in the Amazon delta: Alteration, authigenic clay formation, and storage. *GCA* **2004**, *68*, 1061–1085. [[CrossRef](#)]
151. Cuadros, J. Clay minerals interaction with microorganisms: A review. *Clay Miner.* **2017**, *52*, 235–261. [[CrossRef](#)]
152. Okumura, F.; Mimura, K. Gradual and stepwise pyrolyses of insoluble organic matter from the Murchison meteorite revealing chemical structure and isotopic distribution. *GCA* **2011**, *75*, 7063–7080. [[CrossRef](#)]
153. Remusat, L.; Derenne, S.; Robert, F.; Knicker, H. New pyrolytic and spectroscopic data on Orgueil and Murchison insoluble organic matter: A different origin than soluble? *GCA* **2005**, *69*, 3919–3932. [[CrossRef](#)]
154. Damsté, J.S.S.; Eglinton, T.I.; De Leeuw, J.W.; Schenck, P.A. Organic sulphur in macromolecular sedimentary organic matter: I. Structure and origin of sulphur-containing moieties in kerogen, asphaltenes and coal as revealed by flash pyrolysis. *GCA* **1989**, *53*, 873–889.
155. Baruah, B.; Khare, P. Pyrolysis of high sulfur Indian coals. *Energy Fuels* **2007**, *21*, 3346–3352. [[CrossRef](#)]
156. Xu, L.; Yang, J.; Li, Y.; Liu, J. Behavior of organic sulfur model compounds in pyrolysis under coal-like environment. *Fuel Process. Technol.* **2004**, *85*, 1013–1024. [[CrossRef](#)]
157. Williams, A.; Eigenbrode, J.; Millan, M.; Williams, R.; Buch, A.; Teinturier, S.; Glavin, D.; Freissinet, C.; Szopa, C.; McIntosh, O. Organic Molecules Detected with the First TMAH Wet Chemistry Experiment, Gale Crater, Mars. In Proceedings of the Lunar and Planetary Science Conference, held virtually, 15–19 March 2021; p. 1763.
158. Nachon, M.; Clegg, S.; Mangold, N.; Schröder, S.; Kah, L.; Dromart, G.; Ollila, A.; Johnson, J.; Oehler, D.; Bridges, J. Calcium sulfate veins characterized by ChemCam/*Curiosity* at Gale crater, Mars. *J. Geophys. Res. Planets* **2014**, *119*, 1991–2016. [[CrossRef](#)]
159. Nachon, M.; Mangold, N.; Forni, O.; Kah, L.C.; Cousin, A.; Wiens, R.C.; Anderson, R.; Blaney, D.; Blank, J.G.; Calef, F.; et al. Chemistry of diagenetic features analyzed by ChemCam at Pahrump Hills, Gale crater, Mars. *Icarus* **2017**, *281*, 121–136. [[CrossRef](#)]
160. Caswell, T.E.; Milliken, R.E. Evidence for hydraulic fracturing at Gale crater, Mars: Implications for burial depth of the Yellowknife Bay formation. *EPSL* **2017**, *468*, 72–84. [[CrossRef](#)]
161. Kronyak, R.; Kah, L.; Edgett, K.; VanBommel, S.; Thompson, L.; Wiens, R.; Sun, V.; Nachon, M. Mineral-filled fractures as indicators of multigenerational fluid flow in the Pahrump Hills member of the Murray formation, Gale crater, Mars. *Earth Space Sci.* **2019**, *6*, 238–265. [[CrossRef](#)]
162. Frydenvang, J.; Gasda, P.J.; Hurowitz, J.A.; Grotzinger, J.P.; Wiens, R.C.; Newsom, H.E.; Edgett, K.S.; Watkins, J.; Bridges, J.C.; Maurice, S. Diagenetic silica enrichment and late-stage groundwater activity in Gale crater, Mars. *Geophys. Res. Lett.* **2017**, *44*, 4716–4724. [[CrossRef](#)]
163. Fox, V.; Bennett, K.; Arvidson, R.; Ehlmann, B.; Stack, K.; Dehouck, E.; Grotzinger, J.; Bristow, R.; Salvatore, M.; Catalano, J. Martian clay minerals from orbit to the surface: MSL and MER rover investigations of CRISM smectite detections. *LPI Contrib.* **2019**, *2089*, 6372.
164. Chipera, S.J.; Bish, D.L. *Thermodynamic Modeling of Natural Zeolite Stability*; LA-UR-97-2160; CONF-9706169; Los Alamos National Lab.: Los Alamos, NM, USA, 1997.
165. Blake, D.F.; Hazen, R.M.; Morrison, S.M.; Bristow, T.S.; Sarrazin, P.; Zacny, K.; Rampe, E.B.; Downs, R.T.; Yen, A.; Ming, D.W.; et al. In-Situ Crystallographic Investigations of Solar System Objects in the next Decade. White Paper. 2020. Available online: <https://www.geo.arizona.edu/xtal/group/pdf/01617915314072.pdf> (accessed on 23 July 2021).